machines

MDPI

Article

Multimode Input Shaping for Quay-Side Container Cranes with Multibody-Based Frequency Correction

Gerardo Peláez [1,*,†], Pablo Izquierdo [1,†], Gustavo Peláez [2,†] and Higinio Rubio [3]

[1] Deptartment of Mechanical Engineering, University of Vigo, 36310 Vigo, Spain; pabloizquierdob@uvigo.es
[2] Deptartment of Manufacturing Engineering, University of Vigo, 36310 Vigo, Spain
[3] Deptartment of Mechanical Engineering, University Carlos III of Madrid, 28911 Madrid, Spain; hrubio@ing.uc3m.es
* Correspondence: gpelaez@uvigo.es; Tel.: +34-605066019
† These authors contributed equally to this work.

Abstract

This work investigates multimode vibration suppression in quay-side container cranes by combining analytical modeling, nonlinear multibody simulation, robust Input Shaping, and experimental implementation. A linearized double-pendulum model preserving the main geometric and inertial properties of the spreader–ISO-container assembly is first derived to characterize its coupled dynamics, comprising a low-frequency global pendular mode and a higher-frequency relative ringing mode. The errors introduced by linearization are assessed against a higher-fidelity Simscape Multibody model over a wide range of operating configurations. The comparison shows that the analytical formulation provides sufficiently accurate estimates of the modal frequency ranges for robust shaper design. Two Unity Magnitude One-Hump shapers are therefore synthesized for the identified low- and high-frequency bands and subsequently convolved into a multimode bang–off–bang command. Sensitivity analysis confirms simultaneous attenuation of both target frequency ranges. Numerical validation on the nonlinear multibody model shows that the reduction in residual vibration remains above 90% over the investigated variations in hoisting length and ISO-container center-of-mass position. Finally, a PLC-based laboratory implementation demonstrates that Unity Magnitude shaping can be executed through timed command toggles without online convolution, supporting its practical implementation using conventional industrial control hardware.

Keywords: quay-sidecrane; non-linear multibody simulation; robust input shaping; convolved unity magnitude shaper; convolution free implementation

Check for updates

Academic Editor: Dan Zhang

Received: 28 August 2026
Revised: 22 September 2026
Accepted: 23 September 2026
Published: 26 September 2026

1. Introduction

Quay-side container cranes are essential heavy-duty machines in modern container terminals, providing the lifting and handling capabilities required for the transfer of containers between vessels and the landside transport system. The development of these cranes dates back to 1959, when the first quay crane, known as the *Portainer*, was built by Paceco Corporation and first operated at a marine terminal in Alameda. Since then, quay cranes have evolved considerably, with their size more than doubling in response to the increasing dimensions and capacity of container vessels [1]. According to statistics, approximately 60% of exports and 80% of imports pass through Spanish seaports, representing 53% of Spanish foreign trade with the European Union and 96% with third countries. These figures highlight the strategic importance of quay-side container cranes in the movement of goods, since a substantial fraction of international trade relies on efficient container handling at seaport terminals. More generally, seaports have been reported to handle up to 90% of worldwide goods transportation. Thus, it is not surprising that considerable research effort has been devoted to the identification, modeling, and control of quay-crane dynamics. Louda et al. [2] addressed the identification of load sway frequency in quay cranes, whereas Masoud and Nayfeh [3] investigated sway reduction using a delayed-feedback controller. The influence of hoisting dynamics on anti-sway control performance was subsequently examined in [4], highlighting the relevance of variations in the suspended load configuration when designing effective sway-suppression strategies.

Although quay-side container cranes are essential to container-terminal productivity, the suspended nature of their payload makes them inherently prone to oscillatory motion. Excessive payload sway may increase the risk of collisions with the surrounding infrastructure, reduce positioning accuracy, and ultimately increase container-handling times. Several strategies can be adopted to mitigate these effects. A straightforward solution is to operate the crane at reduced trolley velocities; however, this directly penalizes productivity. Alternatively, closed-loop anti-sway control can be employed, although its implementation requires suitable feedback signals and additional sensing and control infrastructure.

For operator-in-the-loop cranes, command shaping represents a particularly attractive alternative because vibration suppression can be achieved by modifying the reference command before it is applied to the crane, without removing the operator from the control loop. Input Shaping modifies the desired command according to the oscillatory dynamics of the system so that the vibration generated by different portions of the command tends to cancel, thereby reducing transient and residual payload oscillations [5]. Its applicability to crane systems has been demonstrated for operator-generated commands and under variations of the hoisting configuration [6], as well as in operator-in-the-loop crane control architectures [7].

In conventional manually operated quay-side container cranes, the desired trolley motion is introduced by the operator through a joystick, which generates the reference command supplied to the crane drive system. Consequently, the combination of the human operator and the joystick can be regarded as the primary command generator. This architecture provides a natural insertion point for Input Shaping: the operator-generated reference command can be modified in real time before being transmitted to the drive, while preserving the operator's direct control over the crane motion.

Building on the pioneering work of Smith O. J. M. (1957) on Posicast Control [8], Singer and Seering (1990) [5] introduced the concept of Input Shaping, rekindling the interest of the control community in shaping the reference input of flexible mechanical systems such as quay cranes through time-delay filtering. During the past three decades, this renewed interest has led to a substantial body of research devoted to the motion control of vibratory systems. Significant efforts have focused on improving the robustness of input shapers and time-delay filters [9,10], as well as extending their application to multimode multibody systems [11]. Comprehensive reviews of the development of Input Shaping and Time-Delay Filtering over the last five decades can be found in Singhose (2009) [12] and Singh (2009) [13].

In the design of input shapers, several performance criteria must be simultaneously addressed, including robustness, actuator constraints, spectral characteristics, and the time delay introduced by the shaping sequence. The latter becomes particularly critical for quay-side container cranes, whose suspended loads exhibit very low natural frequencies, since robust shapers inevitably require long time-delay filters that may compromise crane productivity. Besides the conventional constrained optimization numerical approach, commonly implemented in the General Algebraic Modeling System (GAMS) Release 25.1.3

to synthesize robust shapers with minimum duration, the design problem can also be reformulated by incorporating a learning-based strategy that compensates for the delay introduced by the shaping sequence [14]. In the proposed approach, the execution of the shaped command remains inherently linked to the crane operator. Specifically, the duration of the shaped command is equal to $T_0 + T_{\mathrm{tail}}$, where T_0 denotes the duration of the unshaped command and T_{tail} is the duration of the input shaper (time-delay filter). Instead of enforcing the shaped command through a fully automated controller, the learning algorithm estimates the appropriate instant at which the operator should release the joystick, ensuring that the complete shaping sequence is executed as intended. Consequently, the human operator becomes an integral part of the control loop, enabling the practical implementation of Input Shaping in industrial quay-crane environments where conventional high-performance feedback control is often difficult to deploy due to the low structural stiffness of the suspended load, the additional flexibility that closed-loop controllers may introduce, and the practical challenges associated with accurately sensing the spreader position under real operating conditions [14].

The pioneering work on this subject is by Peláez et al. [14], where a Unity Magnitude shaper is considered in the standard finite-impulse-response (FIR) filter form. Notice that the Finite Impulse Response FIR filtering of a signal consists of performing the convolution sum operation between the command signal and the digital filter by the system command generator. This work explains how to set up a Real-Time Input Shaping command generator for Quay-Side-Container cranes without carrying out the convolution sum in real time, which represents an unaffordable computational load for the most current and advanced 32-bit microcontrollers and Programmable Logic Controllers, given the challenges and difficulties that arise. In brief, once the switching instants have been determined offline, the primary task of the command generator becomes essentially temporal rather than computational: it only needs to store the prescribed switching instants and accurately execute the corresponding digital toggles. This implementation philosophy clearly distinguishes the proposed approach from a conventional FIR-based input shaper evaluated online, since no real-time convolution operation is required during crane operation.

For sway analysis, a lumped-parameter double-pendulum (2P) representation of the suspended system is adopted. Unlike conventional double-pendulum crane models, in which the hook and payload are treated as point masses [15], the proposed multibody formulation explicitly accounts for the finite dimensions and inertia properties of both the spreader and the ISO-container; thus, the present approach preserves the physical morphology and inertial properties of the two suspended bodies. The hoisting ropes of length ℓ are represented by an equivalent suspension link connecting the trolley to the spreader, while the spreader is modeled as a rigid body of mass m_s, including the container attachment mechanism, constitutes the intermediate body of the double pendulum and provides the articulation point for the ISO-container. The latter is modeled as a rigid body with its own mass m, dimensions, mass moment of inertia, and center of mass located at a finite distance R from the spreader hook. This representation therefore gives rise to two coupled vibration modes: a low-frequency pendular mode primarily associated with the global sway of the suspended assembly and a higher-frequency mode associated with the relative oscillatory motion of the ISO-container with respect to the spreader.

The remainder of this paper is organized as follows. Section 2 develops the dynamic modeling of the suspended quay-crane payload. Starting from the classical single-pendulum representation, a double-pendulum model that preserves the main geometric and inertial properties of the spreader–ISO-container assembly is derived. The corresponding linearized equations of motion and natural frequencies are obtained, and the operational validity of the small-angle approximation is investigated through the dimensionless parameters $\rho = \frac{\ell}{R}$ and $\mu = \frac{m_s}{m}$. A higher-fidelity Simscape Multibody model is subsequently employed to assess the analytical predictions and to identify the frequency variations arising over a wide range of physical operating configurations.

Section 3 addresses the design of the multimode Input Shaping strategy. The frequency ranges identified from both the analytical and multibody analyses are used to define the robustness requirements of two Unity Magnitude One-Hump shapers, respectively tuned to the low-frequency pendular mode and the high-frequency relative ringing mode. Their convolution yields the proposed multimode bang–off–bang shaping command, whose residual-vibration sensitivity and suitability for real-time implementation are subsequently analyzed.

Section 4 evaluates the proposed approach through numerical experiments on the nonlinear multibody model over the complete range of investigated hoisting lengths and spreader–container configurations, comparing shaped and unshaped responses and quantifying the resulting residual-vibration reduction. Also, Section 4.1 presents a laboratory proof-of-concept of the proposed Unity Magnitude shaper implementation, demonstrating the feasibility of the convolution-free, toggle-based execution strategy. Finally, Sections 5 and 6 discuss the main findings and summarize the principal conclusions of the work, respectively. Additional numerical results supporting the comparison between the analytical and multibody natural frequencies are provided in Appendices A and B, as well as the comparison of unshaped and shaped numerical responses in Appendix C.

2. Payload Dynamic Modeling

2.1. Simplified Single Pendulum Model

As stated in [16], which surveys a wide array of dynamic models of boom tower crane rigging systems and their selection criteria, the optimal dynamical model should minimize complexity while preserving sufficient accuracy to meet application requirements. Thus in this section, the payload dynamic modeling is first introduced by comparing the case of an overhead bridge crane operating inside an industrial facility with that of a Quay-Side-Container crane handling standard twenty-foot ISO containers. In typical bridge crane applications, the payload dimensions are often not comparable to those of a container handled by a Quay-Side-Container crane.

Under such conditions, the payload dynamics can, in many cases, be reasonably approximated as a single pendulum, particularly when the distance between the hook and the payload center of mass is relatively small, and the inertial contribution of the hook is negligible compared to that of the payload.

When these assumptions hold, the classical Newtonian model of a simple pendulum can be applied, allowing for a straightforward analysis of the payload dynamics. The bridge crane system considered is illustrated in Figure 1. The payload is suspended from the moving trolley by means of a taut hoisting cable. The trolley motion is prescribed through the independent coordinate x, which is driven by the command input u to reach a desired travelling position r. Therefore, the trolley is not treated as a dynamic body in the present payload-sway analysis, and its mass is not included in the derivation.

The payload is modeled as a point mass m, while ℓ denotes the hoisting cable length. The angular variable Φ represents the deflection of the hoisting cable with respect to the vertical direction, i.e., the payload sway angle.

Assuming negligible damping and considering the hoisting rope to be rigid and massless, the nonlinear equation of motion is obtained by applying Newton's second law in the intrinsic coordinate system $(\vec{e}_\phi, \vec{e}_r)$

$$\vec{e}_\Phi - m\, g\, sin(\Phi) = m\, \ell\, \ddot{\Phi} - m\, \ddot{x}\, cos(\Phi) \quad (1)$$

To ensure safe transportation under real operating conditions, it is typically assumed that $\ddot{x} \ll g$ and that the operator maintains the payload sway angle well below 30°. Under these conditions, the small-angle approximations $\sin(\Phi) \approx \Phi$ and $\cos(\Phi) \approx 1$ can be applied, introducing an approximation error below 5%. Substituting these approximations into the previous nonlinear equation yields the well-known linear ordinary differential equation governing the trolley–payload pendulum system:

$$\ddot{\Phi} + \frac{g}{\ell}\,\Phi = \frac{1}{\ell}\,\ddot{x} \tag{2}$$

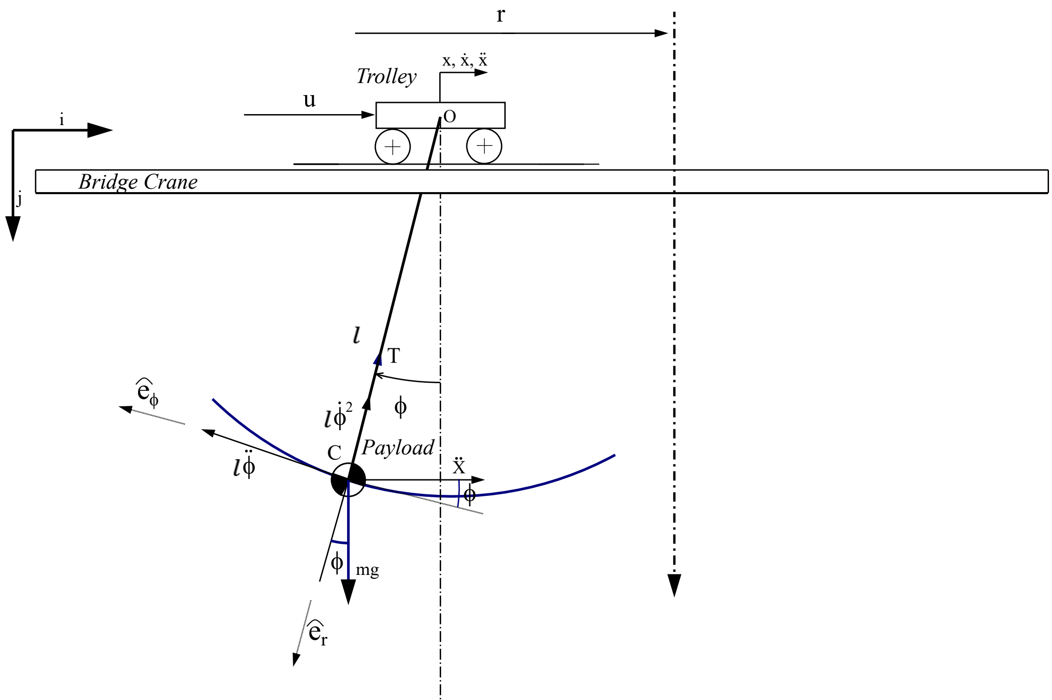

Figure 1. Two-dimensional bridge crane single pendulum dynamic model.

For the system under consideration, the payload dynamics are thus described by a linear second-order differential equation with constant coefficients, whose natural frequency is given by

$$\omega_n = \sqrt{\frac{g}{\ell}}.$$

Starting from the well-known impulse response of a canonical second-order mechanical system with impulse amplitude A, natural frequency ω_n, and damping ratio ζ given by

$$y(t) = \frac{A}{\omega_n\,\sqrt{1-\zeta^2}}\,e^{-\zeta\omega t} sin(\omega_d t + \phi) \tag{3}$$

from Equations (2) and (3), the response of the trolley–payload pendulum undamped system can be readily derived for a unit impulse input $\ddot{x} = \delta$ as follows

$$\Phi(t) = \frac{1}{\sqrt{g\ell}}\sin\left(\sqrt{\frac{g}{\ell}}\,t\right). \tag{4}$$

Nevertheless, the simplicity of the previous formulation relies on modeling the payload as a lumped point mass located at the end of the hoisting cable, thereby neglecting the rotational inertia of the payload about its center of mass.

Such an assumption becomes unrealistic in Quay-Side-Container-crane applications involving standard 20-foot ISO containers, whose dimensions are comparable to the characteristic length scales of the suspended system, as shown in Figure 2. Consequently, neglecting the payload rotational inertia introduces non-negligible modeling errors, since the container moment of inertia significantly increases the equivalent inertia of the suspended system, thereby reducing its swing natural frequency.

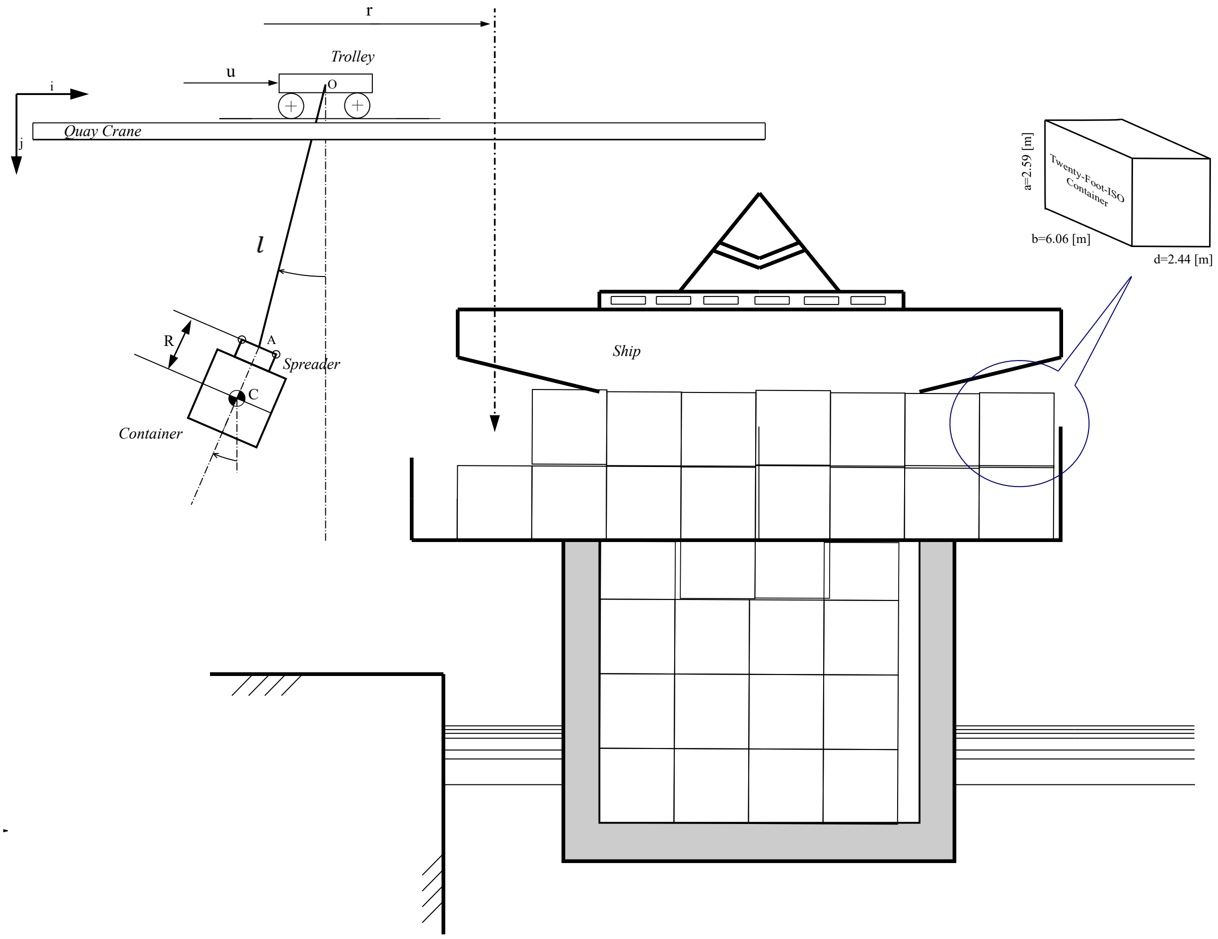

Figure 2. Quay-Side-Container crane suspended container system, where the payload dimensions are no longer negligible with respect to the hoisting length.

2.2. Double-Pendulum Model of a Quay-Side-Container-Crane System Handling a Suspended Spreader–Container Payload.

To analyze the dynamics of the rigid spreader–container assembly, a double-pendulum model is established, as illustrated in Figure 3. In this model, the parameter m denotes the container mass, while ℓ represents the hoisting-cable length. The parameter R corresponds to the distance between the spreader suspension point and the center of mass of the container. The quantity I_c denotes the container moment of inertia about the z-axis, which is perpendicular to the face defined by dimensions a and d. Assuming a uniform mass distribution, this inertia is given by

$$I_c = \frac{1}{12} m(a^2 + d^2). \tag{5}$$

Finally, ϕ represents the swing angle of the hoisting cable, whereas θ denotes the angular deviation of the container center of mass C with respect to the vertical direction. For the purpose of deriving the natural frequencies of the suspended spreader–container system, the trolley suspension point is assumed fixed and taken as the origin of the inertial coordinate frame, $O(0,0)$. This corresponds to the free-vibration condition, in which the trolley motion is removed from the analysis. Assuming negligible damping and a rigid massless hoisting cable, the system kinematics are defined in the inertial coordinate frame shown in Figure 3. Assuming negligible damping and a rigid massless hoisting cable, the system kinematics are defined in the inertial coordinate frame shown in Figure 3. The trolley suspension point is taken as the origin $O(0,0)$. For completeness, the intermediate analytical steps leading from the kinematic description and the Lagrangian formulation to the coupled equations of motion are provided in Appendix A. The resulting linearized equations governing the two generalized coordinates can be written as

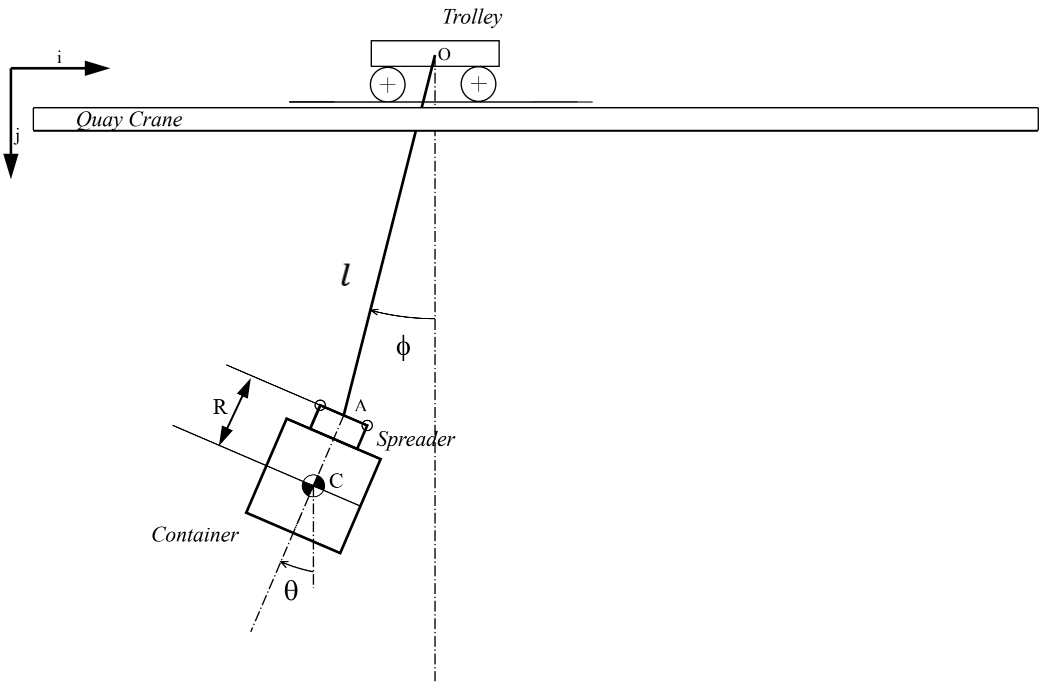

Figure 3. Two-dimensional double-pendulum model of a Quay-Side-Container-crane system handling a suspended spreader–container payload.

$$\begin{aligned} \left(mR^2 + I_C\right)\ddot{\theta} + m\ell R\ddot{\phi} + mgR\theta &= 0, \\ (1+\mu)m\ell^2\ddot{\phi} + m\ell R\ddot{\theta} + (1+\mu)mg\ell\phi &= 0, \end{aligned} \tag{6}$$

where

$$\mu = \frac{m_s}{m},$$

and m_s and m denote the spreader and ISO-container masses, respectively.

To determine the natural frequencies of the suspended spreader–container system, harmonic solutions are assumed for the generalized coordinates:

$$\phi(t) = X_1 \sin(\omega t), \qquad \theta(t) = X_2 \sin(\omega t),$$

where X_1 and X_2 denote the modal amplitudes associated with the swing and rotational modes, respectively. Substituting these harmonic solutions and its derivatives into the corrected linearized Equation (6) of motion yields the following homogeneous algebraic system:

$$\begin{aligned} \left[(1+\mu)mg\ell - (1+\mu)m\ell^2\omega^2\right]X_1 - m\ell R\omega^2 X_2 &= 0, \\ -m\ell R\omega^2 X_1 + \left[mgR - \left(mR^2 + I_C\right)\omega^2\right]X_2 &= 0. \end{aligned} \tag{7}$$

This homogeneous algebraic system can be written in matrix form as

$$\begin{bmatrix} (1+\mu)m\ell(g-\ell\omega^2) & -m\ell R\omega^2 \\ -m\ell R\omega^2 & mgR-(mR^2+I_C)\omega^2 \end{bmatrix} \begin{bmatrix} X_1 \\ X_2 \end{bmatrix} = \begin{bmatrix} 0 \\ 0 \end{bmatrix}. \quad (8)$$

Non-trivial modal solutions exist only if the determinant of the coefficient matrix vanishes:

$$\det \begin{bmatrix} mgR-\omega^2(mR^2+I_C) & -\omega^2 m\ell R \\ -\omega^2 m\ell R & (1+\mu)m\ell(g-\ell\omega^2) \end{bmatrix} = 0.$$

Carrying out the determinant expansion yields

$$\left\{mgR-\omega^2\left(mR^2+I_C\right)\right\}\left\{(1+\mu)m\ell\left(g-\ell\omega^2\right)\right\}-\omega^4 m^2\ell^2R^2=0.$$

After expansion and simplification, the following biquadratic characteristic equation is obtained:

$$\ell\left[(1+\mu)I_C+\mu mR^2\right]\omega^4-g\left[(1+\mu)mR\ell+(1+\mu)I_C+(1+\mu)mR^2\right]\omega^2+(1+\mu)mg^2R=0.$$

dividing by $(1+\mu)\ m$ yields

$$\ell\left[\frac{I_C}{m}+\frac{\mu}{1+\mu}R^2\right]\omega^4-g\left[R\ell+\frac{I_C}{m}+R^2\right]\omega^2+g^2R=0.$$

At this point define

$$\rho=\frac{\ell}{R}, \qquad J_C=\frac{I_C}{mR^2}, \qquad \Omega^2=\frac{\omega^2R}{g}.$$

Then the bicuadratic equation can be rewritten in adimensional mode as follows

$$\rho\left(J_C+\frac{\mu}{1+\mu}\right)\Omega^4-(\rho+J_C+1)\Omega^2+1=0.$$

Let

$$A_\mu=J_C+\frac{\mu}{1+\mu},$$

Substituting yields

$$\rho A_\mu\Omega^4-(\rho+J_C+1)\Omega^2+1=0.$$

Thus, the system natural frequencies are given by

$$\Omega_{1,2}^2=\frac{\rho+J_C+1\mp\sqrt{(\rho+J_C+1)^2-4\rho A_\mu}}{2\rho A_\mu}.$$

Finally

$$\omega_{1,2}=\sqrt{\frac{g}{R}}\Omega_{1,2}, \qquad f_{1,2}=\frac{1}{2\pi}\sqrt{\frac{g}{R}}\Omega_{1,2}.$$

Using the representative quay-side-container-crane operating parameters shown in Table 1, together with a representative ISO-container mass of $m = 22,000$ kg and a spreader mass of $m_s = 6000$ kg, the spreader-to-container mass ratio becomes $\mu = \frac{m_s}{m} = 0.2727$. Substituting these parameters into the proposed analytical formulation yields the following natural frequencies:

$$f_1 \approx 0.0892 \text{ Hz}, \qquad f_2 \approx 0.5024 \text{ Hz}.$$

Table 1. Representative Quay-Side-Container-crane and payload parameters used for the preliminary estimation of the natural frequencies.

Parameter	Value
Hoisting length ℓ	30 [m]
20-foot-ISO Container dimension **a** [1]	2.591 [m]
20-foot-ISO Container dimension **d** [1]	2.438 [m]
Distance from suspension point A to container Mass Center C: **R**	1.5 [m]
ISO-Container mass	22,000 [kg]
Spreader mass	6000 [kg]
$\mu = \frac{m_s}{m}$	0.2727
ρ	20
J_C	0.4688

[1] Standard 20-foot ISO container dimensions

For comparison, the corresponding simple-pendulum frequency for the same hoisting length $\ell = 30$ [m] is

$$f_{sp} = \frac{1}{2\pi}\sqrt{\frac{g}{\ell}} = 0.0910 \text{ Hz}$$

These preliminary results show that the first natural frequency remains very close to the classical pendulum approximation, confirming that the first mode mainly represents the global sway motion of the suspended system. In contrast, the second mode is significantly higher in frequency and is associated with the relative rotational dynamics of the spreader–container assembly. This clear frequency separation provides an initial estimate of the dynamic range that must be considered in the subsequent vibration attenuation strategy.

2.3. *Operational Validity Region of the Small-Angle Linearized Model*

In practical Quay-Side-Container-crane operations, the suspended spreader–container system is excited by the trolley motion. Therefore, the previously derived homogeneous equations of motion must be extended to account for the inertial effects introduced by the trolley acceleration $\ddot{x}(t)$. Within the Lagrangian framework, these effects appear as generalized forcing terms associated with the prescribed horizontal motion of the suspension point.

Under the small-angle assumption, including the horizontal trolley acceleration $\ddot{x}$ as a generalized excitation force in the Lagrange equations, the linearized equations of motion become

$$\begin{aligned} &\left[I_C + (1+\mu)mR^2\right]\ddot{\theta} + m\ell R\ddot{\phi} + mgR\theta = mR\ddot{x}, \\ &(1+\mu)m\ell^2\ddot{\phi} + m\ell R\ddot{\theta} + (1+\mu)mg\ell\phi = (1+\mu)m\ell\ddot{x}. \end{aligned} \tag{9}$$

These equations show that the trolley acceleration acts as an inertial excitation source for both the global sway mode and the rotational mode of the suspended spreader–container assembly. Taking the Laplace transform of the forced linearized equations, assuming zero initial conditions, gives

$$\begin{aligned} &\left\{\left[I_C + (1+\mu)mR^2\right]s^2 + mgR\right\}\Theta(s) + m\ell Rs^2\Phi(s) = mRs^2X(s), \\ &m\ell Rs^2\Theta(s) + \left\{(1+\mu)m\ell^2s^2 + (1+\mu)mg\ell\right\}\Phi(s) = (1+\mu)m\ell s^2X(s). \end{aligned} \tag{10}$$

$$\left(\mathbf{M}s^2 + \mathbf{K}\right)\begin{bmatrix}\Theta(s)\\ \Phi(s)\end{bmatrix} = \mathbf{b}\,\ddot{X}(s),$$

where

$$\mathbf{M} = \begin{bmatrix} I_C + (1+\mu)mR^2 & m\ell\, R \\ m\ell R & (1+\mu)m\ell^2 \end{bmatrix}, \qquad \mathbf{K} = \begin{bmatrix} mgR & 0 \\ 0 & (1+\mu)mg\ell \end{bmatrix},$$

and

$$\mathbf{b} = \begin{bmatrix} mR \\ (1+\mu)m\ell \end{bmatrix}.$$

For a unit impulse trolley acceleration,

$$\ddot{x}(t) = \delta(t), \qquad \ddot{X}(s) = 1.$$

Thus,

$$\begin{bmatrix} \Theta(s) \\ \Phi(s) \end{bmatrix} = \left(\mathbf{M}s^2 + \mathbf{K}\right)^{-1}\mathbf{b}.$$

After carrying out the matrix inversion, the angular responses in the Laplace domain become

$$\Theta(s) = \frac{mR\left[(1+\mu)m\ell^2 s^2 + (1+\mu)mg\ell\right] - (1+\mu)m^2\ell^2 R s^2}{\det\left(\mathbf{M}s^2 + \mathbf{K}\right)},$$

and

$$\Phi(s) = \frac{(1+\mu)m\ell\left[I_C + (1+\mu)mR^2\right]s^2 + (1+\mu)m^2 g\ell R - m^2\ell R^2 s^2}{\det\left(\mathbf{M}s^2 + \mathbf{K}\right)}.$$

Introducing the dimensionless parameters

$$\rho = \frac{\ell}{R}, \qquad \mu = \frac{m_s}{m}, \qquad J_C = \frac{I_C}{mR^2},$$

and the dimensionless time

$$\tau = \sqrt{\frac{g}{R}}\, t,$$

the natural frequencies can be written in dimensionless form as

$$\omega_i = \sqrt{\frac{g}{R}}\, \Omega_i, \qquad i = 1, 2.$$

Defining

$$D_\mu = (1+\mu)(J_C + 1 + \mu) - 1,$$

the dimensionless natural frequencies are obtained from

$$\rho D_\mu \Omega^4 - (1+\mu)(\rho + J_C + 1 + \mu)\Omega^2 + (1+\mu) = 0.$$

Therefore,

$$\Omega_{1,2}^2 = \frac{(1+\mu)(\rho + J_C + 1 + \mu) \mp \sqrt{(1+\mu)^2(\rho + J_C + 1 + \mu)^2 - 4\rho D_\mu (1+\mu)}}{2\rho D_\mu}.$$

For a unit impulse of the normalized trolley acceleration, the impulse response of the relative container angle can be written as

$$\theta(\tau) = A_\theta\left[\frac{\sin(\Omega_1\tau)}{\Omega_1} - \frac{\sin(\Omega_2\tau)}{\Omega_2}\right],$$

where

$$A_\theta = \frac{1+\mu}{\rho D_\mu \left(\Omega_2^2 - \Omega_1^2\right)}.$$

Similarly, the impulse response of the hoisting-cable sway angle is

$$\phi(\tau) = A_{\phi 1}\frac{\sin(\Omega_1 \tau)}{\Omega_1} + A_{\phi 2}\frac{\sin(\Omega_2 \tau)}{\Omega_2},$$

with

$$A_{\phi 1} = \frac{\frac{1+\mu}{D_\mu} - \Omega_1^2}{\rho\left(\Omega_2^2 - \Omega_1^2\right)},$$

and

$$A_{\phi 2} = \frac{\Omega_2^2 - \frac{1+\mu}{D_\mu}}{\rho\left(\Omega_2^2 - \Omega_1^2\right)}.$$

The operational limits of the small-angle formulation were further assessed by applying a unit impulse to the trolley and monitoring the maximum angular excursions of both generalized coordinates, ϕ and θ. Figure 4 identifies the combinations of the dimensionless parameters $\rho = \ell/R$ and $\mu = m_s/m$ for which both angular responses remain within the adopted small-angle threshold,

$$\max|\phi| \leq 10^\circ, \qquad \max|\theta| \leq 10^\circ. \tag{11}$$

For the unit-impulse excitation considered, the small-angle condition is satisfied only for relatively large values of the hoisting-length-to-effective-radius ratio, approximately $\rho \gtrsim 60$, with a comparatively weaker dependence on the spreader-to-container mass ratio μ. This result indicates that ρ is the dominant dimensionless parameter governing the angular excursion under this reference excitation.

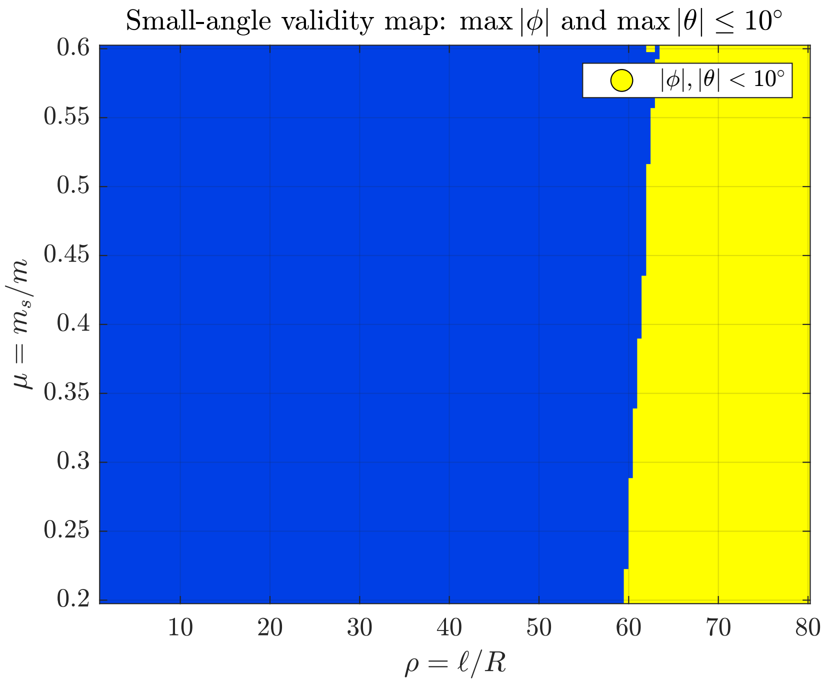

Figure 4. Operational validity region of the small-angle linearized model as a function of the dimensionless parameters ρ and μ, considering hoisting lengths ℓ varying from 5 to 40 m and distances R between the spreader suspension point and the ISO-container from 0.5 to 4 m.The yellow region satisfies the small-angle criterion, whereas the blue region does not.

This limitation is particularly relevant when the dimensionless validity map is compared with the physical parameter range considered for the quay-side container crane. In the present study, the representative operating domain is defined by

$$10\ \text{m} \leq \ell \leq 30\ \text{m}, \qquad 1.295\ \text{m} \leq R \leq 3.295\ \text{m}. \tag{12}$$

Consequently, the corresponding range of the dimensionless geometric ratio is

$$\rho_{\text{min}} = \frac{10}{3.295} \simeq 3.03, \qquad \rho_{\text{max}} = \frac{30}{1.295} \simeq 23.17. \tag{13}$$

Hence, the physically representative operating domain ($3.03 \lesssim \rho \lesssim 23.17$) lies well below the approximate $\rho \simeq 60$ boundary identified in Figure 4 for the unit-impulse small-angle test. Accordingly, the linearized model cannot be expected to reproduce the complete transient response of the suspended assembly over the entire physical operating domain, particularly when the trolley excitation produces appreciable angular excursions.

The analytical formulation should therefore be regarded primarily as a reduced-order model that provides physical insight into the coupled dynamics and first-order estimates of the dominant natural frequencies, rather than as a high-fidelity representation of the complete nonlinear transient response. For this reason, the Simscape Multibody model is subsequently employed to retain the full nonlinear kinematics and geometric coupling of the spreader–container assembly and to evaluate the system response throughout the representative physical operating range. The comparison between the analytical and multibody frequency predictions presented in the following sections also permits the limitations introduced by the linearization to be quantified and motivates the multibody-based frequency correction adopted for the subsequent input-shaper design.

2.4. Multibody-Based Frequency Correction

The two-dimensional multibody model of the quay-crane spreader–container system, adapted from the formulation proposed by Masoud et al. [3], is depicted in Figure 5. The suspended container is handled through a spreader bar connected to the trolley by means of four hoisting cables, two of which are represented in the Figure 5 for clarity.

In this multibody formulation, the trolley motion is prescribed by the operator command through the independent generalized coordinate $u(t)$, whereas the coordinates $x(t)$, $y(t)$, and $\theta(t)$ describe the dependent translational and rotational motion of the container center of mass. Specifically, $x(t)$ and $y(t)$ define the position of the container center of mass in the inertial reference frame, while $\theta(t)$ represents its angular orientation with respect to the vertical direction.

The hoisting cables are modeled as rigid geometric constraints of prescribed length $L(t)$. Consequently, the system kinematics is governed by a set of nonlinear closed-loop constraint equations relating the independent trolley motion to the dependent payload coordinates.

$$\Phi(q,t) = \begin{bmatrix} [x + R\sin\theta - \frac{w}{2}\cos\theta - (u - \frac{d}{2}]^2 + [y - R\cos\theta - \frac{w}{2}\sin\theta]^2 - L^2 \\ [x + R\sin\theta + \frac{w}{2}\cos\theta - (u + \frac{d}{2})]^2 + (y - R\cos\theta + \frac{w}{2}\sin\theta)]^2 - L^2] \end{bmatrix} \tag{14}$$

where w is the transversal dimension of the spreader bar and d is the length of the longitudinal side of the trolley. The dynamic behavior of the constrained multibody system is governed by the well-known differential–algebraic equations (DAEs) formulation,

$$M(q)\ddot{q} - D^T(q,t)\lambda = h^e(q,\dot{q},t), \tag{15}$$

where q is the vector of generalized coordinates, $M(q)$ is the system inertia matrix containing the masses and mass moments of inertia of the rigid bodies, and λ is the vector of Lagrange multipliers associated with the geometric constraint equations.

The matrix

$$D(q,t) = \frac{\partial \Phi(q,t)}{\partial q}$$

is the Jacobian matrix of the kinematic constraint equations, whereas $D^T(q,t)\lambda$ represents the generalized constraint forces enforcing the prescribed cable-length conditions.

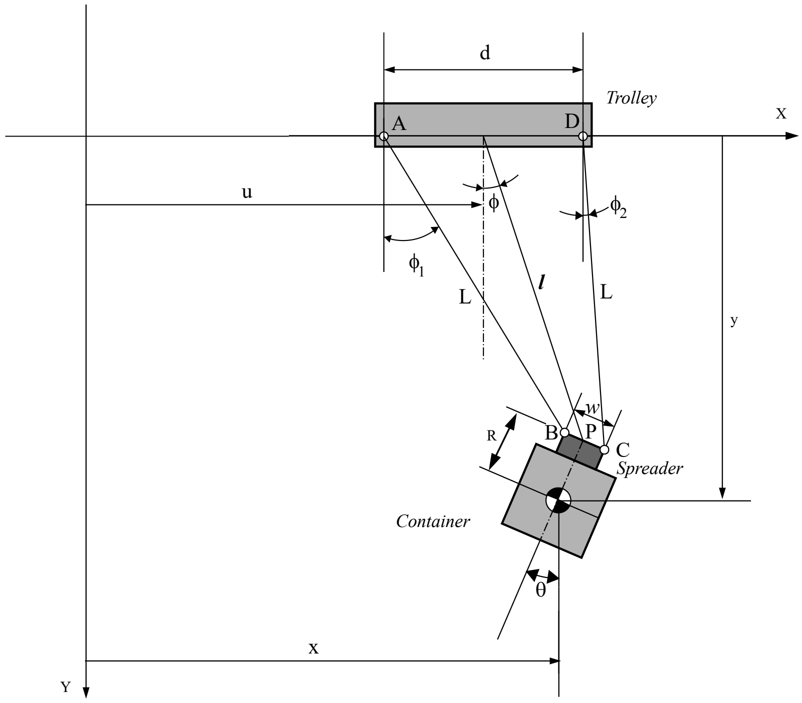

Figure 5. Masoud Multibody Model of a container crane.

Finally, the vector $h^e(q,\dot{q},t)$ gathers the external generalized forces and moments acting on the system, including gravitational effects and the inertial excitation introduced by the trolley motion. If the unknowns are the accelerations $\ddot{q}$ plus the langrange multipliers λ, these equations are treated as linear algebraic equations. However, as in this case the unknowns are the body coordinates (x,y,θ) and the corresponding velocities, the same equations must be treated as second-order differential-algebraic equations (DAE) [17]. Algebraic Equations (15) must be solved for the accelerations. However, there are more unknowns in these equations than the number of equations. To make the number of equations equal to the number of unknowns, the acceleration constraints must be appended and they must be rearranged in matrix form as follows:

$$\begin{aligned} \ddot{\Phi} &= D\ddot{q} + \dot{D}\dot{q} = 0 \\ D\ddot{q} &= -\dot{D}\dot{q} = \gamma \\ \begin{bmatrix} M & -D' \\ D & 0 \end{bmatrix} \begin{bmatrix} \ddot{q} \\ \lambda \end{bmatrix} &= \begin{bmatrix} h^e \\ \gamma \end{bmatrix} \end{aligned} \tag{16}$$

These differential-algebraic equations can be solved numerically for the unknowns $\ddot{q}$ and λ using a multibody simulation framework such as Simscape Multibody (MATLAB R2022a).

Although the analytical linearized model provides valuable physical insight and a first estimate of the natural frequencies of the suspended spreader–container system, its accuracy is limited by the simplifying assumptions adopted in the derivation. In particular, the small-angle approximation, the idealized rigid connections, and the simplified geometric representation of the spreader–container assembly may introduce discrepancies with respect to the actual dynamic behavior of a Quay-Side-Container-crane payload.

To reduce this mismatch, a higher-fidelity multibody model was developed in Simscape Multibody, shown overall in Figure 6. The virtualized Panamax crane consists of a rigid portal-frame structure whose upper beam acts as the linear guide for the trolley, modeled through a prismatic joint. The trolley is connected to the spreader through a revolute joint followed by a rigid coordinate transformation with a variable vertical translation equal to the hoisting length ℓ. The rigid coordinate transformation terminates at the spreader, which is modeled as a rigid body of mass m_s. The spreader is connected to the suspended ISO-container through a second revolute joint followed by a rigid coordinate transformation that translates the reference frame located on the upper face of the spreader to the reference frame attached to the upper face of the ISO-container. The vertical translation is parameterized by the clearance $h_{\text{gap}} = R - a/2$, where $a = 2.59$ m denotes the standardized height of the ISO-container. The latter is represented as a rigid body with standardized dimensions, namely width $d = 2.44$ m, length $b = 6.06$ m, and height $a = 2.59$ m. This multibody formulation preserves the main geometric and inertial characteristics of the suspended spreader–container assembly while maintaining a relatively low computational cost. Consequently, the natural frequencies of both the pendular sway mode and the relative ringing mode can be accurately identified from free-decay or impulsive-response simulations. The reduced-order formulation adopted in this work is intentionally restricted to the planar dynamics associated with the trolley motion and the two dominant oscillatory modes considered for the subsequent Input Shaping design. Actual quay-side container cranes generally employ multiple hoisting ropes attached at different points of the trolley and spreader. In the analytical formulation, the geometric constraints introduced by the two rope pairs visible in the plane of motion are retained following the multi-rope modeling assumptions commonly adopted for quay-side container cranes [3]. The hoisting ropes are assumed to be massless, inextensible links of constant length. Consistently with this assumption, the Simscape Multibody representation reproduces the corresponding suspension geometry through rigid frame transformations and revolute joints, rather than by explicitly modeling the axial elasticity and distributed dynamics of each individual rope.

This representation is appropriate for the objective of the present study, namely the identification and attenuation of the low-frequency global pendular mode and the higher-frequency relative spreader–container ringing mode excited by the commanded trolley motion. Nevertheless, it does not constitute a complete spatial model of the actual multi-rope suspension system. In particular, out-of-plane sway, rotation about the vertical axis (yaw), rope elasticity, and possible torsional modes resulting from asymmetric loading or rope dynamics are not represented. These effects therefore define an applicability limit of the proposed reduced-order model and would require an extended three-dimensional multi-rope formulation if their dynamics were to be explicitly investigated.

Wind loading represents a different limitation because it constitutes an external disturbance rather than a vibration generated by the prescribed trolley command. Input Shaping is a feedforward command-generation technique: it reduces residual vibration by preventing the commanded motion from exciting the targeted oscillatory modes, but it does not provide disturbance rejection against unmeasured external excitations. Consequently, wind-induced sway or yaw cannot, in general, be actively suppressed by the proposed feedforward shaper alone. Rejection of such disturbances would require the addition of a feedback control layer together with appropriate sensing of the relevant spreader–container motion. A combined Input-Shaping/feedback architecture therefore represents a possible extension when rejection of external disturbances is required.

The natural frequencies extracted from the Simscape Multibody model were compared with those predicted by the linearized double-pendulum formulation. This comparison was used to assess the validity of the reduced-order analytical model over a range of hoisting lengths and container center-of-mass locations.

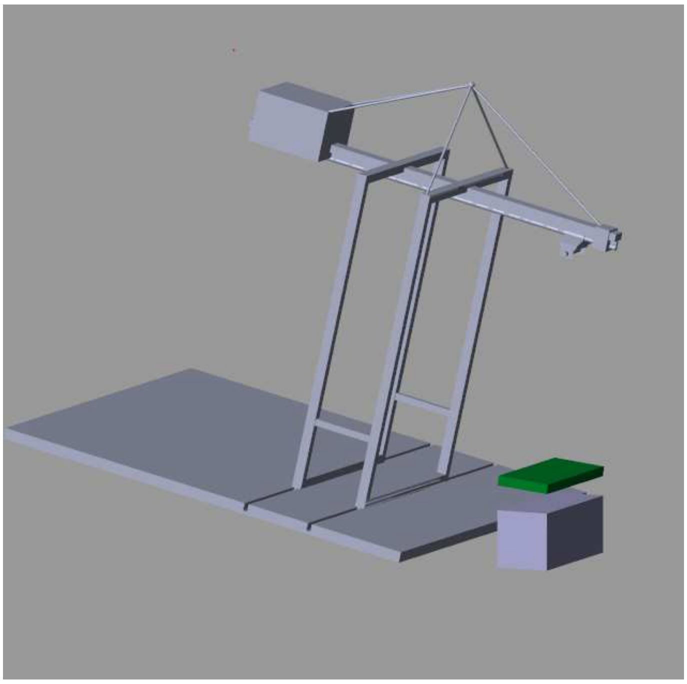

(**a**)

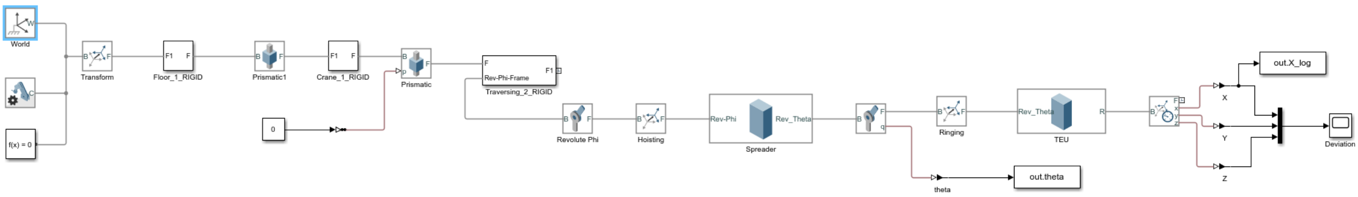

(**b**)

Figure 6. Simscape Multibody representation of the quay crane trolley–spreader–container system used for dynamic analysis and validation of the proposed input-shaping strategy. (**a**) Mechanical Explorer visualization of the Simscape Multibody model of the quay crane trolley–spreader–container system. (**b**) General view of the Simscape implementation employed for the dynamic analysis and validation of the proposed input-shaping strategy.

Regarding the overall results shown in Figure 7, the low-frequency mode f_1 was estimated from the Simscape Multibody model by imposing a small initial perturbation of 2° on the generalized coordinate Φ, while maintaining the trolley fixed. The resulting oscillatory response was obtained from the horizontal displacement of the ISO-container center of mass and subsequently processed through FFT analysis.

$$X_c \approx \ell\,\Phi + R\,\theta$$

The comparison between the analytical model and the Simscape Multibody results shows that the analytical formulation predicts the first natural frequency with excellent accuracy throughout the physically admissible range of ρ. The slight increase observed in the first natural frequency as the parameter $\rho = \frac{\ell}{R}$ increases can be explained from a physical standpoint. Since the hoisting length ℓ = 30 [m] is kept constant throughout the parametric study, increasing ρ implies a reduction in the distance R between the spreader attachment point and the ISO-container center of mass. As R decreases, the contribution of the relative rotational motion to the overall displacement of the ISO-container center of mass becomes progressively smaller. Consequently, the global motion of the suspended system approaches that of a single equivalent pendulum. At the same time, the effective position of the combined spreader–container center of mass moves closer to the main suspension point, slightly reducing the effective pendulum length associated with the global hoisting mode. Since the natural frequency of a pendular system is inversely proportional to the square root of its effective length, the reduction of the equivalent pendulum length produces a small increase in the first natural frequency, which is consistent with both the analytical predictions and the multibody simulation results.

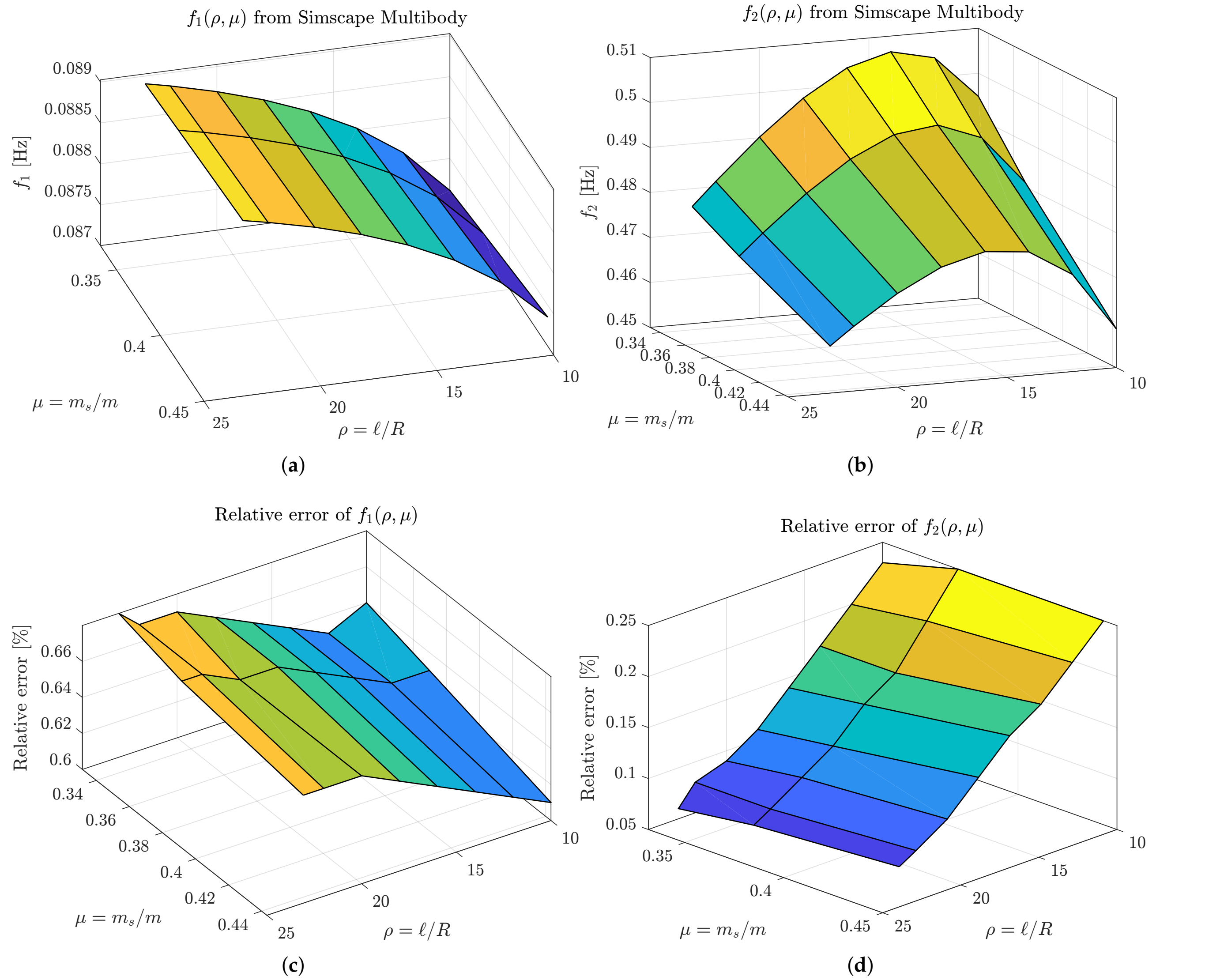

Figure 7. Comparison between analytical and Simscape Multibody natural frequencies for different values of $\rho = \ell/R$ and $\mu = m_s/m$. (**a**) Low-frequency mode f_1 as a function of the dimensionless parameters $\rho = \ell/R$ and $\mu = m_s/m$. (**b**) Low-frequency mode f_2 as a function of the dimensionless parameters $\rho = \ell/R$ and $\mu = m_s/m$. (**c**) Relative error of the low-frequency mode f_1 between the analytical linearized model and the Simscape Multibody estimation. (**d**) Relative error of the high-frequency mode f_2 between the analytical linearized model and the Simscape Multibody estimation.Warmer colors indicate higher values of the represented quantity, whereas cooler colors indicate lower values.

Similarly, the high-frequency mode f_2 was estimated by imposing a small initial perturbation on the generalized coordinate θ. In this case, the FFT analysis was performed on the relative angular deflection of the ISO-container center of mass with respect to the vertical direction. The high-frequency mode is weakly observable in the global translational motion of the payload and is therefore better identified through the relative angular motion between the spreader and the container. The obtained frequencies were then compared against the analytical predictions derived from the linearized ordinary differential equation model. As observed in Figure 7, the agreement between the analytical model and the multibody simulations improves as the parameter $\rho = \frac{\ell}{R}$ increases, whose relative error decreases from approximately 0.22% to below 0.1%. Physically, larger values of ρ correspond to smaller distances between the spreader attachment point and the ISO-container center of mass, thereby reducing the amplitude of the relative rotational motion and increasing the validity of the small-angle assumptions adopted in the linearized analytical derivation.

The dimensionless parameters $\rho = \ell/R$ and $\mu = m_s/m$ were introduced to assess the validity of the analytical linearization over the range of operating conditions considered in this work. Since the proposed Input Shaping strategy effectively limits the oscillation amplitudes of both generalized coordinates, the small-angle assumptions adopted for ϕ and θ remain valid during crane operation. Consequently, the analytical natural frequencies obtained from the linearized ordinary differential equations closely match those extracted from the nonlinear Simscape Multibody model.

As reported in Table 2 and Appendix B (Table A1), when the hoisting length is kept constant at $\ell = 30$ m and the parameters ρ and μ are varied by modifying the ISO-container mass-center-to-spreader distance R and the ISO-container mass, respectively, the maximum relative deviation between the analytical and numerical predictions remains below 0.68% for the low-frequency mode (f_1) and below 0.25% for the high-frequency mode (f_2). These discrepancies are remarkably small and mainly serve to validate the proposed linearized analytical model under small-amplitude oscillations.

For more representative quay-crane operating conditions, where both the hoisting length ℓ and the distance R vary simultaneously during ship-to-truck loading and unloading operations, larger discrepancies are naturally observed as reported in Table 3. These results are also reported more precisely in Appendix C (Table A2), reflecting the increasing influence of the nonlinear multibody dynamics as the operating range is extended.

Table 2. Variation ranges and mean values of the identified natural frequencies obtained from the Simscape Multibody model over the analyzed domain of the dimensionless parameters ρ and μ.

Mode	Minimum (Hz)	Mean (Hz)	Maximum (Hz)	Relative Variation (%)
Low-frequency mode (f_1)	0.087004	0.088293	0.089027	2.29
High-frequency mode (f_2)	0.458620	0.489991	0.520304	12.59

Table 3. Variation ranges and mean values of the identified natural frequencies obtained by varying the physical operating parameters of the Simscape Multibody model, namely the hoisting length $\ell \in [10, 30]$ m and the ISO-container mass-center-to-spreader distance $R \in [1.295, 3.295]$ m.

Mode	Minimum (Hz)	Mean (Hz)	Maximum (Hz)	Relative Variation (%)
Low-frequency mode (f_1)	0.085449	0.110107	0.146484	55.43
High-frequency mode (f_2)	0.482178	0.518921	0.555420	14.11

3. Transition-Based Bang–Off–Bang Shaping Commands

Extracted from the above analysis of the dynamic responses obtained from the Simscape Multibody model of the ISO-container quay crane system, the proposed convolved

https://doi.org/10.3390/machines14101104

Multimode Unity Magnitude input shaper must attenuate the vibration amplitudes associated with both the low-frequency pendular mode and the high-frequency relative ringing mode over the complete range of identified natural frequencies. To maximize the robustness of the proposed shaping strategy, the design frequency intervals were selected by considering the envelope defined by the two validation methodologies presented in Appendices A and B, namely the proposed dimensionless parameterization (ρ, μ) and the validation performed by varying the physical operating parameters of the Simscape Multibody model, namely the hoisting length ℓ and the ISO-container mass-center-to-spreader distance R. Consequently, the design interval adopted for the low-frequency mode was

$$f_1 \in [0.085449,\ 0.146484] \text{ Hz},$$

which corresponds to the widest frequency excursion obtained when the physical operating parameters of the Simscape Multibody model were varied. For the high-frequency relative ringing mode, the adopted design interval was

$$f_2 \in [0.458620,\ 0.555420] \text{ Hz},$$

where the minimum frequency was obtained from the proposed dimensionless formulation, whereas the maximum frequency was obtained from the validation based on the physical operating parameters of the Simscape Multibody model. By adopting the extreme frequencies identified from both validation procedures, the proposed multimodal input shaper was designed to provide robust vibration suppression for all operating configurations that may arise from the wide range of parameter variations investigated throughout this work.

For speed-critical applications such as port unloading operations, where the time that a vessel remains berthed must be minimized, bang–off–bang acceleration commands constitute a particularly appealing option. In this context, a unity-magnitude input shaper is adopted, generating motion commands that deviate from classical bang–bang profiles. Specifically, the resulting commands follow a bang–off–bang structure in which all acceleration pulses are strictly non-negative, thereby avoiding reverse (negative) acceleration phases that may be perceived as undesirable by crane operators.

These shaping commands correspond to sequences of digital ON/OFF transitions that approximate the desired acceleration profile while maintaining a very low computational burden and a short implementation time. Consequently, the proposed Unity Magnitude shapers can be regarded as a particular class of digital bang–off–bang shaping commands, mathematically described as

$$u(t) = u_i, \qquad T_i \le t < T_{i+1}, \qquad i = 0, 1, \ldots, r-1, \tag{17}$$

where

$$u_i \in \{0, 1\}, \tag{18}$$

denotes the discrete actuator state, with $u_i = 1$ corresponding to the ON state and $u_i = 0$ to the OFF state. The transition instants T_i define the switching times between consecutive actuator states, while r denotes the total number of digital transitions composing the shaping command. When commanding an ISO-container quay crane, each transition in the acceleration profile excites oscillations of the suspended load, typically involving the dominant sway modes of the trolley–spreader–container system. If the timing of these transitions is carefully chosen by a skilled operator, the residual oscillations at the end of the maneuver can be significantly reduced or even eliminated.

In practice, operators often rely on an empirical strategy consisting of positioning the trolley in alignment with the spreader trajectory, effectively minimizing sway through experience-based timing adjustments. This approach represents the de facto operating "law" followed in manual crane control.

Alternatively, real-time Input Shaping can be employed by acting directly on the operator-generated command transitions, rather than predefining a complete motion profile. In this approach, the sequence of shaping pulses—restricted to non-negative amplitudes—is generated in real time and synchronized with the duration of the operator input. Specifically, both the activation (start) and deactivation (stop) transitions of the trolley motion are shaped so as to attenuate the inertial excitation of the suspended load, thereby reducing residual oscillations without requiring explicit trajectory planning.

Note that in practical implementations, the control input is typically provided as a velocity reference to the drive system. However, due to the fast inner-loop dynamics of modern motor drives, the resulting acceleration closely follows the time derivative of the commanded velocity. Therefore, the acceleration-based input shaping framework remains a valid and effective approximation for vibration suppression. This can be expressed as

$$\begin{aligned} v_{ref}(t) = \dot{v}(t) = u(t) \\ a(t) = \dot{v}_{ref} \end{aligned} \tag{19}$$

Using the representative operating conditions summarized in Table 2, two Unity Magnitude One-Hump input shapers were designed based on the mean values of the identified natural frequencies, namely $f_1 = 0.1160$ Hz and $f_2 = 0.5070$ Hz. Each input shaper was tuned to suppress one of the two dominant vibration modes of the suspended ISO-container, namely the global pendular mode and the relative ringing mode. In brief, the low-frequency shaper captures the global motion of the trolley–spreader–container system, while the high-frequency shaper accounts for the relative oscillation of the ISO container with respect to the spreader. The Unity Magnitude shapers employed in this work were designed following the tabulated synthesis procedure proposed by Pao and Singhose [18].

$$\begin{bmatrix} A_i \\ T_i \end{bmatrix}_{f_{1\ low}:0.1160\ Hz} = \begin{bmatrix} 1 & -1 & 1 & -1 & 1 \\ 0 & 0.8219 & 3.1697 & 5.5517 & 6.3504 \end{bmatrix}$$

$$\begin{bmatrix} A_i \\ T_i \end{bmatrix}_{f_{2\ high}:0.5070 Hz} = \begin{bmatrix} 1 & -1 & 1 & -1 & 1 \\ 0 & 0.1880 & 0.7252 & 1.2702 & 1.4529 \end{bmatrix}$$

As illustrated in Figure 8, the proposed convolved Unity Magnitude shaper provides excellent attenuation over the low-frequency pendular mode. The residual vibration remains well below the prescribed tolerance of 5% throughout almost the entire target frequency interval $f_1 \in [0.085449,\ 0.146484]$ Hz. Only in the vicinity of the upper frequency bound does the residual vibration increase slightly above the tolerance level, with the insensitive region extending approximately up to 0.140 Hz. Considering the limited width of this transition region, the resulting performance degradation is negligibly small for practical crane operation.

The convolution of both shaping sequences results in the 25-tap multi-mode bang–off–bang command listed in Table 4 and illustrated in Figure 9. This command is capable of simultaneously attenuating both the low-frequency pendular mode and the high-frequency relative ringing mode.

The attenuation characteristics of the high-frequency ringing mode exhibit a small residual ripple compared with those of the individual Unity Magnitude shaper tuned to the high-frequency mode shown in Figure 10b. This behavior is not introduced by the convolution process itself but arises from the off-design sensitivity of the low-frequency

Unity Magnitude shaper, whose residual-vibration response exceeds 100% in the high-frequency range. Since the residual-vibration sensitivity of the convolved shaper is equal to the product of the individual residual-vibration sensitivities divided by 100 as follows,

$$V_{\text{conv}}(\omega) = \frac{V_{\text{low}}(\omega)\, V_{\text{high}}(\omega)}{100} \tag{20}$$

the off-design amplification of the low-frequency shaper slightly deteriorates the attenuation capability of the high-frequency shaper. This property is verified in Figure 10a, which shows the residual-vibration sensitivity of the low-frequency Unity Magnitude shaper, and in Figure 10c, where the sensitivity curve obtained directly from the convolved shaper is shown to coincide with the product of the individual sensitivity curves.

Table 4. Convolved multi-mode bang–off–bang shaping command. The table reports the sequence of taps and their corresponding activation times.

Tap Amplitude	Time (s)
+1	0.000
−1	0.188
+1	0.725
−1	0.822
+1	1.009
−1	1.270
+1	1.453
−1	1.546
+1	2.091
−1	2.274
+1	3.170
−1	3.357
+1	3.894
−1	4.439
+1	4.622
−1	5.552
+1	5.739
−1	6.276
+1	6.350
−1	6.537
+1	6.821
−1	7.004
+1	7.074
−1	7.619
+1	7.802

The resulting shaped velocity command is illustrated in Figure 9. An important feature of the proposed Convolved Unity Magnitude shaper is that the resulting command retains a bang–off–bang structure, switching exclusively between $U_{\max}$ and zero. Therefore, once the shaping times have been computed, real-time evaluation of the convolution sum is no longer required. Instead, the digital command generator only needs to store the sequence of shaping times and toggle the output between U_{max} and OFF whenever each prescribed switching instant is reached. This event-based implementation substantially reduces the computational burden of the real-time command generator, since no convolution operations have to be carried out within the execution window of the periodic interrupt. This is particularly advantageous for embedded implementations based on 32-bit microcontrollers or Programmable Logic Controllers (PLCs), where an excessive computational load within the timed interrupt may lead to interrupt overlap or timing violations.

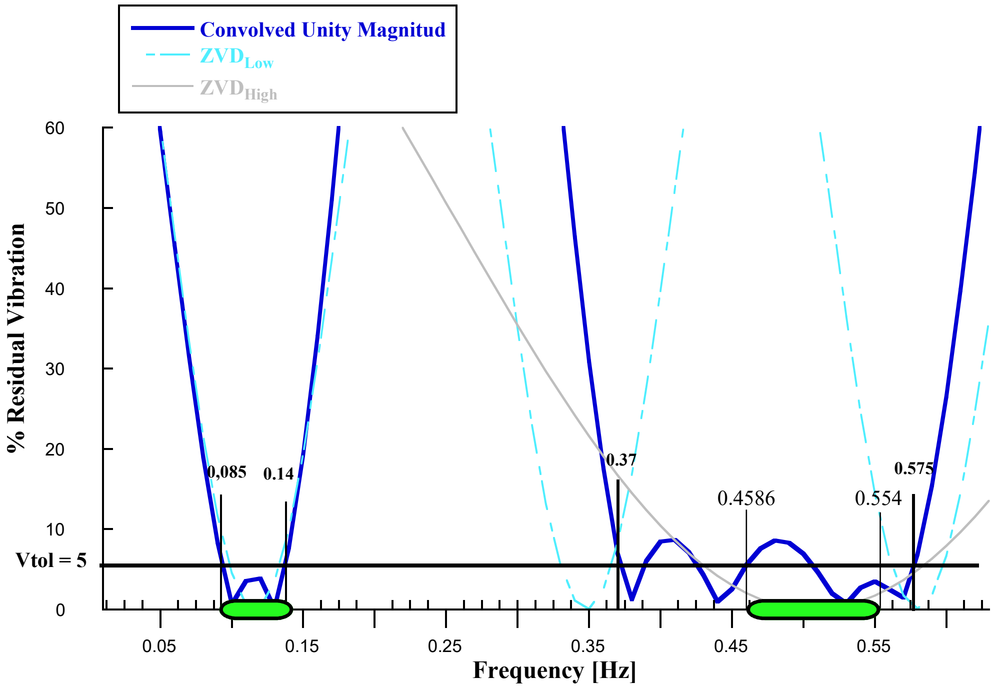

Figure 8. Residual vibration sensitivity curve of the proposed convolved multimode Unity Magnitude input shaper. The sensitivity curves of the individual low-frequency and high-frequency ZVD shapers are included for comparison. The highlighted frequency bands correspond to the target attenuation intervals identified from the multibody simulations and encompass the extreme natural frequencies arising from the complete set of operating configurations analyzed in this work.

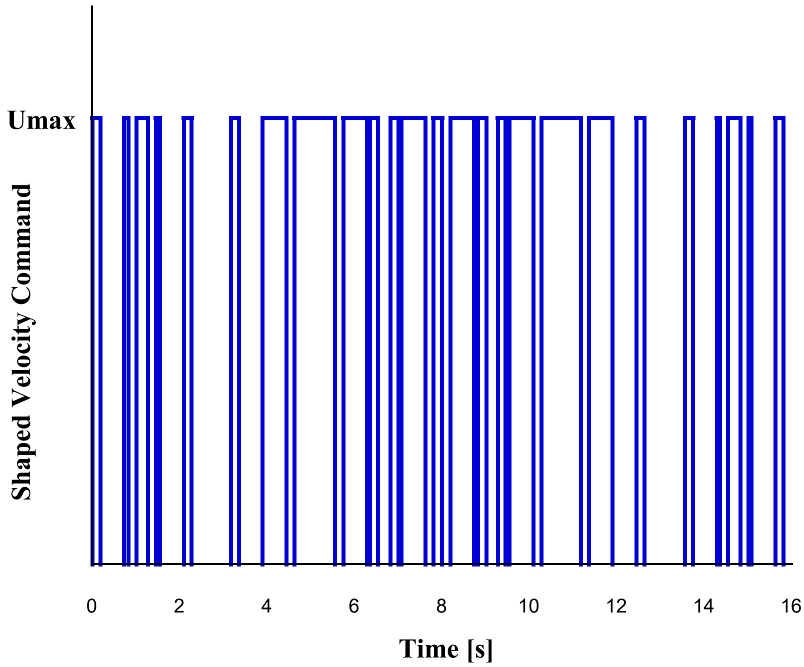

Figure 9. Convolved Unity Magnitude shaped velocity command implemented as a sequence of bang–off–bang switching events between U_{max} and OFF. The prescribed shaping times can therefore be implemented as output toggles without evaluating the convolution sum in real time.

A further practical advantage of this command structure is its close correspondence with the operating strategy naturally adopted by quay-crane operators. During conventional unshaped operation, experienced operators typically apply successive trolley velocity corrections in an attempt to bring the trolley toward the instantaneous position of the suspended spreader and thereby manually reduce its oscillation. The bang–off–bang shaped command preserves this intuitive sequence of motion and pause intervals, while determining the switching instants systematically from the vibration-suppression shaper. Consequently, the proposed implementation can be interpreted as a digitally timed counterpart of the corrective maneuver that operators already perform manually, rather than as an entirely different crane-motion strategy.

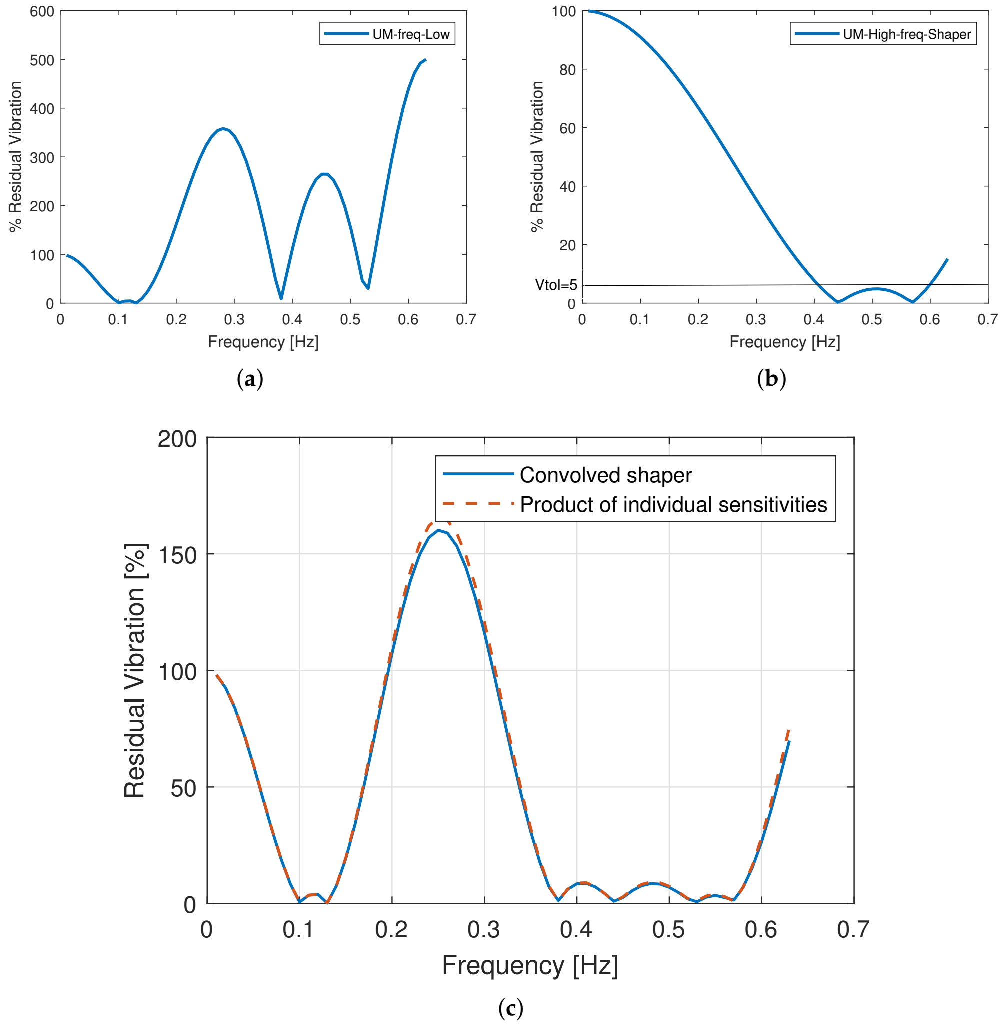

Figure 10. Residual-vibration sensitivity analysis of the proposed multimode Unity Magnitude shaping strategy. (**a**) Sensitivity of the Unity Magnitude shaper tuned to the low-frequency pendular mode (Residual-vibration sensitivity of the Low-frequency Unity Magnitude shaper). (**b**) Sensitivity of the Unity Magnitude shaper tuned to the high-frequency relative ringing mode (Residual-vibration sensitivity of the High-frequency Unity Magnitude shaper). (**c**) Residual-vibration sensitivity of the convolved Unity Magnitude shaper together with the product of the individual sensitivity curves, demonstrating that the response of the convolved shaper is accurately described by the product of the individual sensitivities (Residual-vibration sensitivity of the convolved Unity Magnitude shaper together with the product of the individual sensitivity curves).

4. Results

4.1. Analytical vs. Multibody Results

The comparison between the analytical and Multibody results provides further insight into both the capabilities and the limitations of the linearized formulation. As discussed in Section 2.3, the response of the analytical model to a unit-impulse trolley excitation shows that the angular excursions of ϕ and θ do not necessarily remain within the adopted small-angle threshold of 10° over the physically representative ranges of the dimensionless parameters ρ and μ. Consequently, the small-angle formulation cannot be expected to reproduce the complete transient response of the suspended spreader–container assembly under operating conditions involving appreciable angular excursions. This observation provides a first motivation for complementing the analytical formulation with the nonlinear Simscape Multibody model, in which the full geometric kinematics of the suspended assembly are retained.

Nevertheless, an important result is that this limitation in the prediction of the complete transient response does not prevent the linearized model from providing highly accurate estimates of the natural frequencies. The dominant frequencies extracted by FFT from the logged angular responses ϕ and θ of the Multibody model remain within the frequency ranges predicted by the analytical formulation throughout the investigated parameter domain. More specifically, the maximum relative deviation between the analytical and Multibody predictions remains below 0.68% for the low-frequency mode f_1 and below 0.25% for the high-frequency mode f_2. Such small discrepancies confirm that the linearized analytical model provides an accurate representation of the modal frequencies, even though the small-angle assumption may cease to be representative of the complete finite-amplitude transient response under the unit-impulse excitation.

The combined analytical and Multibody parametric analyses also permit representative frequency-variation intervals to be established for the two coupled vibration modes. By systematically varying the dimensionless parameters ρ and μ, together with the physically representative geometric parameters ℓ and R, the frequency excursions relevant to the subsequent robust shaper design were identified. For the low-frequency global pendular mode, the adopted interval is

$$f_1 \in [0.085449,\ 0.146484]\ \mathrm{Hz}, \tag{21}$$

which corresponds to the widest frequency excursion obtained when the physical operating parameters of the Simscape Multibody model were varied. For the high-frequency relative spreader–container mode, the adopted design interval is

$$f_2 \in [0.458620,\ 0.555420]\ \mathrm{Hz}. \tag{22}$$

These intervals are particularly relevant from a control-design perspective, since they provide the frequency bounds used to define the two Unity Magnitude shapers subsequently combined into the 25-tap multimode command. The parametric analysis therefore serves not only to characterize the variability of the coupled crane dynamics, but also to translate the analytical and Multibody modeling results into explicit frequency-domain requirements for the robust input-shaping design. The analytical and Multibody formulations should therefore be regarded as complementary rather than alternative descriptions of the crane dynamics. The analytical model provides a compact physical interpretation of the coupled modes and accurately predicts their natural-frequency ranges, whereas the Multibody model permits the resulting finite-amplitude motion to be evaluated without imposing the small-angle kinematic approximation. This distinction is particularly relevant for the subsequent input-shaping analysis: the analytical formulation establishes the underlying modal structure and expected frequency variation, while the Multibody model provides the higher-fidelity dynamic environment in which the performance and robustness of the multimode shaping strategy are assessed over the representative crane operating domain.

4.2. Shaping-Performance Results

This subsection evaluates the effectiveness of the proposed convolved Unity Magnitude shaper through numerical simulations performed on the nonlinear Simscape Multibody model. The objective is to compare the dynamic responses obtained with conventional unshaped commands and with the proposed shaping strategy, assessing its capability to suppress both the low-frequency pendular mode and the high-frequency relative ringing mode while preserving the desired trolley motion.

The virtual trolley was commanded to travel 16 m along the translational prismatic joint. The unshaped motion was generated using a constant position increment of 0.002 m at a sampling period of 1 ms, corresponding to an equivalent trolley velocity of 2 m/s over an 8 s maneuver. For the shaped case, the same incremental command was processed by the 25-tap Convolved Unity Magnitude shaper prior to cumulative integration, resulting in a piecewise-linear position command while preserving the same final displacement. After completion of the trolley motion, the final position was maintained for an additional 20 s to allow the residual payload oscillations to evolve freely. As shown in the overall Figure 11, the 25-tap Convolved Unity Magnitude shaper provides a substantial reduction in the peak-to-peak residual vibration over the complete range of physical parameters ℓ and R considered in the Multibody model. Figure 11a quantifies this improvement in terms of residual-vibration reduction, which remains approximately within the 90–100% range throughout the investigated parameter domain and exceeds approximately 95% over a substantial portion of it. The corresponding absolute peak-to-peak amplitudes are shown in Figure 11b, where the continuous curves represent the unshaped responses and the dashed curves the shaped responses. The separation between both sets of curves becomes particularly pronounced for the larger hoisting lengths. For $\ell = 20$ m, the unshaped peak-to-peak residual vibration is approximately 4.7–5.7 m over the investigated range of R, whereas the shaped response remains below approximately 0.3 m. At $\ell = 25$ m, the corresponding unshaped amplitudes increase to approximately 7.9–9.0 m, while the shaped responses remain below approximately 0.6 m. Finally, for $\ell = 30$ m, the unshaped residual vibration reaches approximately 10.8–11.6 m, compared with only approximately 0.9–1.3 m after application of the multimode command. Therefore, despite the strong increase in the unshaped vibration amplitude with hoisting length, the shaped response remains comparatively small. The combined results of Figure 11a,b thus demonstrates both quantitatively, and in terms of absolute suspended-load displacement, the effectiveness of the proposed 25-tap multimode command over substantially different crane configurations. Also an interesting feature can nevertheless be observed in the unshaped responses for a hoisting length of approximately $\ell = 15$ m, for which the residual vibration exhibits a pronounced minimum for all the investigated values of R. This behavior can be explained by the particular relationship between the duration of the trolley maneuver and the dominant low-frequency pendular dynamics. The unshaped 16 m displacement is performed at an equivalent constant velocity of 2 m/s over 8 s; therefore, the abrupt velocity changes at the beginning and end of the motion constitute the two principal excitation events of the pendular mode. For $\ell = 15$ m, the phase accumulated by this mode during the 8 s trolley motion approaches a condition for destructive interference between the oscillatory responses generated by these two events. Consequently, the vibration excited at the beginning of the maneuver is partially canceled by that induced when the trolley stops, producing the pronounced minimum observed in the unshaped residual response. This effect should not be interpreted as an intrinsically favorable dynamic condition of the crane, since it results from a fortuitous matching between the maneuver duration and the modal frequency and is therefore highly sensitive to changes in the operating conditions. In contrast, the shaped responses remain consistently low throughout the complete (ℓ,R) parameter sweep, demonstrating that the vibration reduction achieved by the proposed shaping strategy does not rely on such an accidental phase-cancellation condition.

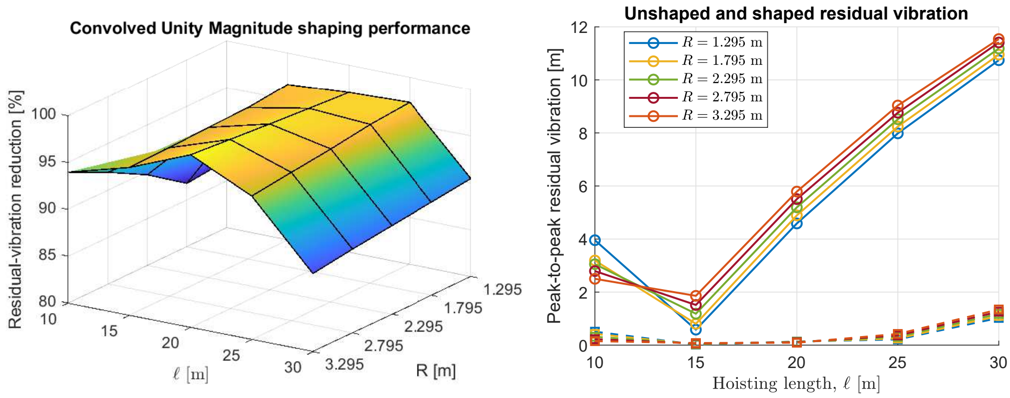

(**a**) (**b**)

Figure 11. Performance of the Convolved Unity Magnitude input shaper over the complete (ℓ, R) parameter sweep. In (**a**), warmer colors indicate higher residual-vibration reduction, whereas cooler colors indicate lower reduction. In (**b**), solid and dashed lines represent the unshaped and shaped responses, respectively, with colors identifying the different values of R indicated in the legend. (**a**) Percentage reduction in residual vibration with respect to the unshaped response (Residual-vibration reduction achieved by the Convolved Unity Magnitude shaper over the complete set of physical parameters ℓ and R). (**b**) Direct comparison of the peak-to-peak residual vibration amplitudes obtained with the unshaped and shaped commands (Peak-to-peak residual vibration amplitude for the unshaped and Convolved Unity Magnitude shaped responses as a function of the hoisting length ℓ and parameter R. A logarithmic scale is used for the vertical axis to facilitate comparison between the substantially different residual-vibration amplitudes of the unshaped and shaped responses).

4.3. Laboratory Proof-of-Concept of the Unity Magnitude Shaper Implementation

It should be emphasized that this laboratory demonstrator is not intended to reproduce the multimode dynamics of the quay-crane spreader–ISO-container assembly. Rather, it is employed as an experimental proof-of-concept of the proposed Unity Magnitude shaping implementation and of its capability to attenuate residual oscillations in a real suspended-load system.

The overall Figure 12 provides a laboratory proof-of-concept of the vibration-suppression capability of the Unity-Magnitude shaping strategy. Figure 12a shows the unshaped trolley motion, where the successive positions recorded during the forward displacement define the commanded transport trajectory. Once the trolley reaches its final position, the abrupt termination of the unshaped motion excites a pronounced oscillatory response of the suspended mass, as shown in Figure 12b, with horizontal displacement amplitudes reaching approximately 0.75 m. In contrast, Figure 12c shows the trolley trajectory resulting from the time integration of the velocity command shaped by the Unity-Magnitude input shaper. The corresponding response of the suspended mass, shown in Figure 12d, exhibits a substantial attenuation of the oscillatory motion. In particular, once the shaped trolley maneuver is completed, the residual vibration amplitude is reduced to approximately 0.10 m, demonstrating the effectiveness of the Unity-Magnitude shaping strategy in suppressing the vibration induced by the transport motion.

The trolley velocity command was implemented using a Siemens S7-200 CPU-214 PLC (Siemens, Munich, Germany), which provides the timing required to execute the Unity-Magnitude switching sequence. The PLC output drives a relay-based power stage that controls the direction and energization of a Crouzet DC motor responsible for the trolley motion. Despite the deliberately simple and low-cost nature of the experimental platform, the resulting dynamic performance is remarkably effective. In particular, the experiment illustrates that implementation of the Unity-Magnitude shaper does not require online convolution or computationally intensive real-time filtering. Once the switching instants have been calculated, the fundamental task of the command generator is essentially temporal: the switching instants are stored and the corresponding command toggles are accurately executed by the PLC. The substantial reduction in residual oscillation observed in Figure 12d therefore provides an experimental proof-of-concept of the practical implementability of the proposed shaping strategy using conventional industrial control hardware. It should be noted, however, that the laboratory demonstrator is not intended to constitute a dynamically scaled representation of an industrial quay-side container crane. Therefore, the experimental reduction in residual vibration observed in the laboratory setup should not be directly extrapolated in magnitude to a full-scale Panamax crane. The role of the experiment is instead to demonstrate the hardware implementability of the proposed convolution-free Unity Magnitude command-generation strategy, whereas the dynamic performance over representative full-scale operating conditions is assessed through the nonlinear Simscape Multibody model presented in the preceding sections.

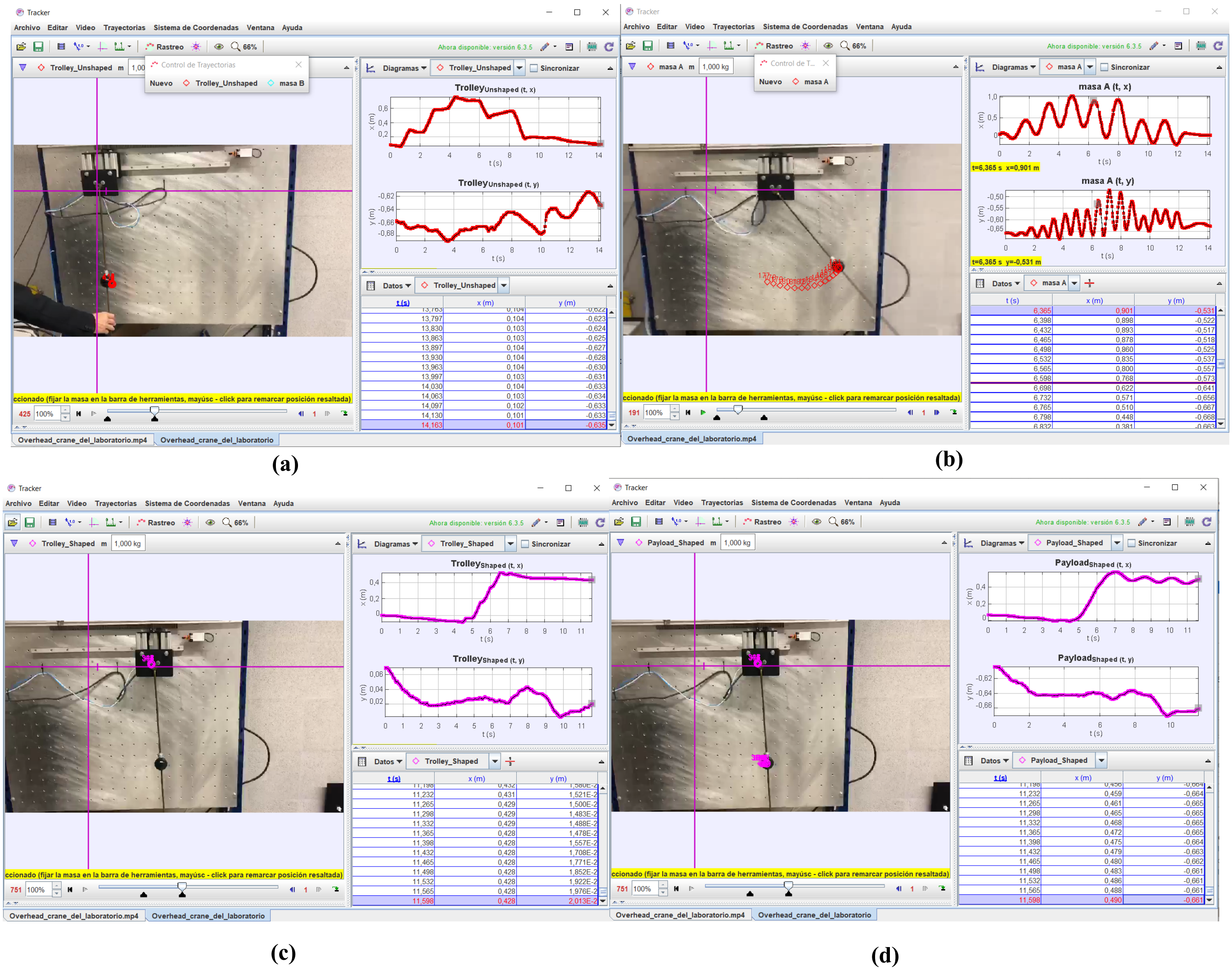

Figure 12. Laboratory proof-of-concept comparing unshaped and Unity-Magnitude shaped trolley commands and the corresponding suspended-payload responses: (**a**) unshaped trolley motion command; (**b**) resulting suspended-payload response, showing the residual oscillations induced by the unshaped trolley motion; (**c**) Unity-Magnitude shaped motion command, producing the prescribed trolley displacement through a smooth position evolution; and (**d**) corresponding suspended-payload response, showing the suppression of residual vibration after completion of the trolley motion.

For an eventual industrial implementation, the use of a conventional PLC inside the trolley operator cabin is not considered essential. Although modern industrial PLCs provide sufficient computational capability, the restricted installation space available at the operator console and the relatively small number of signals required by the proposed command generator favor a more compact embedded implementation. In particular, a PSoC 5LP-based controller is considered a suitable candidate for implementing the timed Unity Magnitude toggles. The required digital I/O comprises the absolute-encoder data and direction signals, the safety-relay signal, the shaped/unshaped mode selection, and the corresponding command and indication outputs. Since the proposed implementation does not perform online convolution, its real-time computational requirement is limited essentially to monitoring the relevant inputs, maintaining the maneuver timing, and executing the precomputed command transitions at their prescribed instants.

A compact touchscreen HMI like M5Stack can additionally be incorporated as a supervisory interface without participating in the deterministic execution of the shaper. Following the learning-assisted implementation concept, the controller can measure and store the characteristic maneuver time, while the HMI displays the remaining maneuver time and indicates to the operator the appropriate instant at which the joystick should be released. The remaining portion of the command is then completed by the terminal sequence of the Unity Magnitude shaper, allowing the residual suspended-load vibration to be canceled while preserving the operator-in-the-loop architecture. This embedded implementation therefore provides a feasible route for transferring the proposed shaping strategy to an industrial crane while requiring only limited additional hardware in the operator cabin.

5. Discussion

From a practical implementation standpoint, the proposed Convolved Unity Magnitude shaper does not require the convolution operation to be evaluated in real time. Once the convolution of the individual low- and high-frequency shapers has been performed offline, the resulting switching instants listed in Table 4 can be stored directly in the command generator. Real-time execution therefore becomes essentially a temporal rather than computational task, consisting of accurately reproducing the prescribed transitions between $U_{\max}$ and OFF. This substantially reduces the computational burden imposed on the embedded control platform and distinguishes the proposed implementation from a conventional FIR-based input shaper evaluated online.

Nevertheless, the use of the complete multimode shaper introduces a relatively large number of command transitions. Whether all these transitions can be faithfully reproduced in an actual quay-crane installation depends on the dynamic and switching characteristics of the available trolley drive, including its internal hysteresis, dead times, and bandwidth. Closely spaced transitions may not be individually reproduced and could effectively overlap at the drive level. Consequently, the implementation should be adapted to the specific drive installed on the crane. When the drive dynamics permit accurate reproduction of the complete switching sequence, the convolved shaper provides simultaneous attenuation of both identified vibration modes. Conversely, when the switching capability of the drive constitutes a limiting factor, the low-frequency Unity Magnitude shaper may be implemented alone, considerably reducing the number of required transitions while retaining suppression of the dominant global pendular sway mode.

6. Conclusions

This work has developed and assessed a multimode Input Shaping strategy specifically conceived for the coupled oscillatory dynamics of the suspended spreader–ISO-container assembly of a quay-side container crane. The main contribution is the integration of a physically representative analytical description of the suspended assembly, a higher-fidelity nonlinear Simscape Multibody model, robust multimode Unity Magnitude shaping, and a convolution-free implementation concept suitable for industrial command generation.

A distinctive feature of the proposed modeling approach is that the spreader and the ISO-container are explicitly represented as rigid bodies with their relevant geometric and inertial properties. In contrast with conventional double-pendulum crane formulations in which the hook and payload are commonly idealized as point masses, the present formulation preserves the distributed inertia and relative geometry of the actual spreader–container assembly. This representation reveals two clearly separated coupled vibration modes: a low-frequency mode associated primarily with the global pendular sway of the suspended assembly and a higher-frequency mode associated with the relative ringing motion of the ISO-container with respect to the spreader. The resulting reduced-order formulation therefore provides a direct physical basis for identifying the two frequency ranges that must be simultaneously attenuated by the multimode shaper.

The comparison with the nonlinear Simscape Multibody model also clarifies the scope of the analytical formulation. The unit-impulse analysis showed that the angular excursions can exceed the adopted 10° small-angle threshold over physically representative configurations, and consequently the linearized model should not be interpreted as a high-fidelity predictor of the complete finite-amplitude transient response. Nevertheless, its prediction of the modal frequencies was remarkably accurate: the maximum relative deviations with respect to the Multibody results remained below 0.68% for the low-frequency mode f_1 and below 0.25% for the high-frequency mode f_2. This distinction constitutes an important result of the study: a reduced-order linearized model may remain highly effective for modal characterization and robust shaper synthesis even when a nonlinear Multibody representation is required to reproduce the complete finite-amplitude motion.

The combined analytical and Multibody parametric analyses established the design intervals

$$f_1 \in [0.085449,\ 0.146484]\ \text{Hz}, \qquad f_2 \in [0.458620,\ 0.555420]\ \text{Hz}, \tag{23}$$

for the low- and high-frequency modes, respectively. These intervals were used to design two robust One-Hump Unity Magnitude shapers, whose convolution produced the proposed 25-tap multimode bang–off–bang command. The resulting sequence simultaneously addresses both vibration mechanisms while preserving the Unity Magnitude command structure. The residual-vibration sensitivity analysis further showed that the robustness of the convolved sequence can be interpreted directly through the product of the sensitivities of the individual shapers, providing a useful link between the individual modal designs and the resulting multimode attenuation capability.

Evaluation on the nonlinear Multibody model demonstrated that the 25-tap command maintains substantial vibration attenuation throughout the investigated physical parameter domain. Residual-vibration reduction remained approximately within the 90–100% range and exceeded approximately 95% over a substantial portion of the investigated configurations. More importantly, the absolute shaped residual amplitudes remained comparatively small even as the corresponding unshaped oscillations increased markedly with hoisting length. For example, at $\ell = 30$ m, unshaped peak-to-peak residual vibrations of approximately 10.8–11.6 m were reduced to approximately 0.9–1.3 m. These results indicate that the substantial frequency variability produced by changes in the suspended configuration can be accommodated by a fixed robust multimode command without requiring continuous online retuning of the shaper.

The laboratory experiments provide a complementary proof-of-concept of the command-generation principle rather than a dynamically scaled reproduction of a full-size quay-side container crane. They demonstrate that, once the convolved switching sequence has been calculated offline, the Unity Magnitude command can be executed as a deterministic sequence of timed digital transitions without evaluating the FIR convolution sum in real time. This feature considerably reduces the computational requirements of the control platform and facilitates its transfer to compact industrial hardware. For a future crane implementation, a PSoC 5LP-based embedded controller is envisaged as a suitable candidate for deterministic execution of the timed toggles, with the necessary industrial signal conditioning and isolation. A compact touchscreen HMI, such as an M5Stack device, could operate independently as a supervisory interface for displaying the learned maneuver time, the remaining command time, and the appropriate joystick-release instant, while leaving the real-time execution of the shaper to the dedicated controller. This architecture preserves the operator-in-the-loop nature of the crane while requiring only limited additional hardware in the operator cabin.

Future work will therefore focus on transferring the proposed architecture from the present proof-of-concept to a full-scale quay-side container crane. This will include the development and industrial conditioning of the compact embedded controller, integration with the existing joystick, direction, encoder, and safety signals, and implementation of the learning-assisted maneuver-timing strategy and supervisory HMI. Particular attention will also be devoted to experimentally assessing the influence of drive bandwidth, dead times, hysteresis, and minimum admissible switching intervals on the execution of the complete 25-tap command. Full-scale tests will ultimately permit the robustness predicted by the Multibody simulations to be evaluated under actual variations in hoisting length, suspended mass, operating conditions, and operator-command timing.

Overall, the proposed methodology establishes a direct path from the physical modeling of the spreader–ISO-container assembly to the identification of the relevant modal-frequency intervals, the synthesis of a robust multimode Unity Magnitude command, and its computationally inexpensive implementation. The combination of explicit rigid-body modeling, Multibody validation, robust two-mode shaping, and deterministic convolution-free command generation provides a practical framework for suppressing both global sway and relative spreader–container ringing in operator-controlled quay-side container cranes.

Author Contributions: Conceptualization, G.P. (Gerardo Peláez) and P.I.; methodology, G.P. (Gerardo Peláez); software, G.P. (Gerardo Peláez); validation, G.P. (Gerardo Peláez), P.I. and H.R.; formal analysis, G.P. (Gustavo Peláez); investigation, G.P. (Gerardo Peláez); resources, P.I.; data curation, G.P. (Gustavo Peláez); writing—original draft preparation, G.P. (Gerardo Peláez); writing—review and editing, G.P. (Gerardo Peláez); visualization, G.P. (Gerardo Peláez); supervision, G.P. (Gustavo Peláez); project administration, G.P. (Gustavo Peláez); funding acquisition, G.P. (Gustavo Peláez). All authors have read and agreed to the published version of the manuscript.

Funding: This research received no external funding.

Data Availability Statement: The original contributions presented in this study are included in the article. Further inquiries can be directed to the corresponding author.

Conflicts of Interest: The authors declare no conflicts of interest.

Abbreviations

The following abbreviations are used in this manuscript:

FFT	Fast Fourier Transform
ODE	Ordinary Differential Equation
UM	Unity Magnitude

Appendix A. Detailed Derivation of the Reduced-Order Analytical Model

This appendix provides the intermediate mathematical steps omitted from Section 2.2 for conciseness. Starting from the kinematic relations and the kinetic and potential energies of the spreader–container assembly, the Lagrangian formulation is developed to obtain the coupled equations of motion used in the main text. The coordinates of the spreader suspension point A are given by

$$\mathbf{r}_A = \begin{bmatrix} -\ell \sin\phi \\ \ell \cos\phi \end{bmatrix}.$$

The position vector from point A to the container center of mass C is expressed as

$$\mathbf{r}_{AC} = R \begin{bmatrix} -\sin\theta \\ \cos\theta \end{bmatrix}.$$

Consequently, the position vector of the container center of mass is

$$\mathbf{r}_C = \mathbf{r}_A + \mathbf{r}_{AC} = \begin{bmatrix} -\ell \sin\phi - R\sin\theta \\ \ell\cos\phi + R\cos\theta \end{bmatrix}.$$

Thus,

$$\mathbf{v}_C = \mathbf{v}_A + \boldsymbol{\omega} \times \mathbf{r}_{AC},$$

with

$$\boldsymbol{\omega} = \dot{\theta}\,\mathbf{k}.$$

According to the adopted coordinate system, the velocity of point A, where the spreader mass is assumed to be concentrated, is given by

$$\mathbf{v}_A = \begin{bmatrix} -\ell\dot{\phi}\cos\phi \\ -\ell\dot{\phi}\sin\phi \end{bmatrix},$$

The ISO-container center of mass C is located at a distance R from the spreader-hook point A, whereas the rotational contribution is

$$\boldsymbol{\omega} \times \mathbf{r}_{AC} = R\dot{\theta} \begin{bmatrix} -\cos\theta \\ -\sin\theta \end{bmatrix}.$$

Therefore, the velocity of the container center of mass becomes

$$\mathbf{v}_C = \begin{bmatrix} -\ell\dot{\phi}\cos\phi - R\dot{\theta}\cos\theta \\ -\ell\dot{\phi}\sin\phi - R\dot{\theta}\sin\theta \end{bmatrix}.$$

After straightforward manipulation,

$$\mathbf{v}_C^T \mathbf{v}_C = \ell^2\dot{\phi}^2 + R^2\dot{\theta}^2 + 2\ell R\dot{\phi}\dot{\theta}\cos(\phi - \theta).$$

The kinetic energy is composed of three contributions: the translational kinetic energy of the spreader, whose mass is assumed to be concentrated at point A; the translational kinetic energy of the ISO-container center of mass C; and the rotational kinetic energy associated with the relative rotation θ of the ISO-container about its center of mass. Under this assumption, the spreader contribution is fully accounted for through its translational kinetic energy and therefore does not contribute to the rotational inertia associated with the coordinate θ.

The spreader-to-container mass ratio is defined as

$$\mu = \frac{m_s}{m},$$

where m_s and m denote the spreader and ISO-container masses, respectively.

Accordingly, the kinetic energy can be written as

$$T = \frac{1}{2} m_s \, \mathbf{v}_A^T \mathbf{v}_A + \frac{1}{2} m \, \mathbf{v}_C^T \mathbf{v}_C + \frac{1}{2} I_C \dot{\theta}^2.$$

Using $m_s = \mu m$, and expanding the velocity terms, this expression becomes

$$T = \frac{1}{2}(1+\mu) m \ell^2 \dot{\phi}^2 + \frac{1}{2}\Big(mR^2 + I_C\Big)\dot{\theta}^2 + m\ell R \dot{\phi}\dot{\theta}\cos(\phi - \theta).$$

Assuming small oscillations around the vertical equilibrium configuration, the term

$$\cos(\phi - \theta)$$

appearing in the kinetic energy expression can be expanded as

$$\cos(\phi - \theta) = 1 - \frac{1}{2}(\phi - \theta)^2 + \mathcal{O}\Big((\phi - \theta)^4\Big).$$

Therefore, within a first-order linearized model, the higher-order terms can be neglected and

$$\cos(\phi - \theta) \simeq 1.$$

Thus, under the small-oscillation assumption, the kinetic energy reduces to

$$T = \frac{1}{2}(1+\mu) m \ell^2 \dot{\phi}^2 + \frac{1}{2}\Big(mR^2 + I_C\Big)\dot{\theta}^2 + m\ell R \dot{\phi}\dot{\theta}.$$

The gravitational potential energy of the suspended spreader–container system is given by

$$V = -mg[(1+\mu)\ell\cos\phi + R\cos\theta],$$

where the sign convention follows from the adopted coordinate system, whose vertical axis is positive downward. Therefore, the Lagrangian of the system becomes

$$\mathcal{L} = T - V,$$

that is, the Lagrangian of the spreader–container system becomes

$$\mathcal{L} = \frac{1}{2}(1+\mu) m \ell^2 \dot{\phi}^2 + \frac{1}{2}\Big(mR^2 + I_C\Big)\dot{\theta}^2 + m\ell R \dot{\phi}\dot{\theta} + mg[(1+\mu)\ell\cos\phi + R\cos\theta].$$

The Euler–Lagrange equations are then obtained from

$$\frac{d}{dt}\left(\frac{\partial \mathcal{L}}{\partial \dot{q}_i}\right) - \frac{\partial \mathcal{L}}{\partial q_i} = 0,$$

with generalized coordinates

$$q_1 = \phi, \qquad q_2 = \theta.$$

Finally, after applying the Euler–Lagrange equations, the small-angle approximations

$$\sin\phi \simeq \phi, \qquad \sin\theta \simeq \theta$$

are introduced in the restoring terms in order to obtain the linearized system dynamics as follows:

$$\begin{aligned} \left(mR^2 + I_C\right)\ddot{\theta} + m\ell R\ddot{\phi} + mgR\theta = 0, \\ (1+\mu)m\ell^2\ddot{\phi} + m\ell R\ddot{\theta} + (1+\mu)mg\ell\phi = 0. \end{aligned} \tag{A1}$$

To determine the natural frequencies of the suspended spreader–container system, harmonic solutions are assumed for the generalized coordinates:

$$\phi(t) = X_1 \sin(\omega t), \qquad \theta(t) = X_2 \sin(\omega t),$$

where X_1 and X_2 denote the modal amplitudes associated with the swing and rotational modes, respectively.

Their first- and second-order time derivatives are therefore given by

$$\dot{\phi}(t) = X_1\omega\cos(\omega t), \qquad \ddot{\phi}(t) = -\omega^2 X_1 \sin(\omega t),$$

and

$$\dot{\theta}(t) = X_2\omega\cos(\omega t), \qquad \ddot{\theta}(t) = -\omega^2 X_2 \sin(\omega t).$$

Substituting these harmonic solutions into the corrected linearized Equation (A1) of motion yields the following homogeneous algebraic system:

$$\begin{aligned} \left[(1+\mu)mg\ell - (1+\mu)m\ell^2\omega^2\right]X_1 - m\ell R\omega^2 X_2 = 0, \\ -m\ell R\omega^2 X_1 + \left[mgR - \left(mR^2 + I_C\right)\omega^2\right]X_2 = 0. \end{aligned} \tag{A2}$$

This homogeneous algebraic system can be written in matrix form as

$$\begin{bmatrix} (1+\mu)m\ell(g - \ell\omega^2) & -m\ell R\omega^2 \\ -m\ell R\omega^2 & mgR - (mR^2 + I_C)\omega^2 \end{bmatrix} \begin{bmatrix} X_1 \\ X_2 \end{bmatrix} = \begin{bmatrix} 0 \\ 0 \end{bmatrix}. \tag{A3}$$

Non-trivial modal solutions exist only if the determinant of the coefficient matrix vanishes:

$$\det\begin{bmatrix} mgR - \omega^2(mR^2 + I_C) & -\omega^2 m\ell R \\ -\omega^2 m\ell R & (1+\mu)m\ell(g - \ell\omega^2) \end{bmatrix} = 0.$$

Carrying out the determinant expansion yields

$$\left\{mgR - \omega^2\left(mR^2 + I_C\right)\right\}\left\{(1+\mu)m\ell\left(g - \ell\omega^2\right)\right\} - \omega^4 m^2\ell^2 R^2 = 0.$$

After expansion and simplification, the following biquadratic characteristic equation is obtained:

$$\ell\left[(1+\mu)I_C + \mu mR^2\right]\omega^4 - g\left[(1+\mu)mR\ell + (1+\mu)I_C + (1+\mu)mR^2\right]\omega^2 + (1+\mu)mg^2R = 0.$$

Dividing by $(1+\mu)\ m$ yields

$$\ell\left[\frac{I_C}{m} + \frac{\mu}{1+\mu}R^2\right]\omega^4 - g\left[R\ell + \frac{I_C}{m} + R^2\right]\omega^2 + g^2R = 0.$$

At this point define

$$\rho = \frac{\ell}{R}, \qquad J_C = \frac{I_C}{mR^2}, \qquad \Omega^2 = \frac{\omega^2 R}{g}.$$

Then the bicuadratic equation can be rewritten in adimensional mode as follows:

$$\rho\left(J_C + \frac{\mu}{1+\mu}\right)\Omega^4 - (\rho + J_C + 1)\Omega^2 + 1 = 0.$$

Let

$$A_\mu = J_C + \frac{\mu}{1+\mu}.$$

Substituting yields

$$\rho A_\mu \Omega^4 - (\rho + J_C + 1)\Omega^2 + 1 = 0.$$

Thus, the system natural frequencies are given by

$$\Omega_{1,2}^2 = \frac{\rho + J_C + 1 \mp \sqrt{(\rho + J_C + 1)^2 - 4\rho A_\mu}}{2\rho A_\mu}.$$

Finally,

$$\omega_{1,2} = \sqrt{\frac{g}{R}}\Omega_{1,2}, \qquad f_{1,2} = \frac{1}{2\pi}\sqrt{\frac{g}{R}}\Omega_{1,2}.$$

Appendix B. Validation of the Proposed Dimensionless Formulation

The proposed analytical formulation was validated over the complete range of the dimensionless parameters $\rho = \ell/R$ and $\mu = m_s/m$ considered in this work.

For all simulations reported in Table A1, the hoisting length was kept constant at $\ell = 30$ m, while the parameter ρ was modified exclusively by changing the ISO-container mass-center-to-spreader distance R. Consequently, the variation in the natural frequencies reported in this appendix is solely associated with the changes in the dimensionless parameters ρ and μ.

Table A1 summarizes the analytical natural frequencies, the frequencies identified from the Simscape Multibody simulations, and the corresponding relative errors for all analyzed configurations.

Table A1. Comparison between the analytical natural frequencies and the frequencies identified from the Simscape Multibody model for the complete set of analyzed values of the dimensionless parameters $\rho = \ell/R$ and $\mu = m_s/m$.

ρ	μ	R (m)	ℓ (m)	f_1 (Hz)	f_2 (Hz)	$f_{1,a}$ (Hz)	$f_{2,a}$ (Hz)	Error f_1 (%)	Error f_2 (%)
10	0.2896	3.0000	30	0.087004	0.512795	0.087480	0.511646	0.540	0.22
12	0.2896	2.5000	30	0.087559	0.520174	0.088055	0.519195	0.560	0.19
14	0.2896	2.1429	30	0.087946	0.520304	0.088468	0.519488	0.590	0.16
16	0.2896	1.8750	30	0.088234	0.515713	0.088778	0.515053	0.610	0.13
18	0.2896	1.6667	30	0.088458	0.508185	0.089020	0.507662	0.630	0.10
20	0.2896	1.5000	30	0.088638	0.498912	0.089214	0.498514	0.650	0.08
22	0.2896	1.3636	30	0.088786	0.488703	0.089373	0.488415	0.660	0.06
23.0769	0.2896	1.3000	30	0.088855	0.483016	0.089447	0.482781	0.660	0.05
10	0.33158	3.0000	30	0.087109	0.494883	0.087667	0.493729	0.640	0.23
12	0.33158	2.5000	30	0.087646	0.504303	0.088202	0.503302	0.630	0.20
14	0.33158	2.1429	30	0.088021	0.506497	0.088589	0.505635	0.640	0.17
16	0.33158	1.8750	30	0.088301	0.503790	0.088880	0.503089	0.650	0.14
18	0.33158	1.6667	30	0.088519	0.497926	0.089108	0.497369	0.660	0.11
20	0.33158	1.5000	30	0.088694	0.490124	0.089291	0.489661	0.670	0.09
22	0.33158	1.3636	30	0.088839	0.481148	0.089442	0.480784	0.670	0.08
23.0769	0.33158	1.3000	30	0.088906	0.476027	0.089512	0.475727	0.680	0.06

Table A1. *Cont.*

ρ	μ	R (m)	ℓ (m)	f_1 (Hz)	f_2 (Hz)	$f_{1,a}$ (Hz)	$f_{2,a}$ (Hz)	Error f_1 (%)	Error f_2 (%)
10	0.36966	3.0000	30	0.087197	0.480956	0.087749	0.479780	0.630	0.25
12	0.36966	2.5000	30	0.087720	0.491802	0.088273	0.490786	0.630	0.21
14	0.36966	2.1429	30	0.088086	0.495477	0.088650	0.494612	0.640	0.17
16	0.36966	1.8750	30	0.088359	0.494224	0.088935	0.493484	0.650	0.15
18	0.36966	1.6667	30	0.088572	0.489632	0.089157	0.489039	0.660	0.12
20	0.36966	1.5000	30	0.088743	0.482914	0.089336	0.482448	0.660	0.10
22	0.36966	1.3636	30	0.088884	0.474926	0.089483	0.474532	0.670	0.08
23.0769	0.36966	1.3000	30	0.088949	0.470254	0.089551	0.469932	0.670	0.07
10	0.44320	3.0000	30	0.087355	0.458620	0.087896	0.457488	0.610	0.25
12	0.44320	2.5000	30	0.087852	0.471572	0.088398	0.470531	0.620	0.22
14	0.44320	2.1429	30	0.088201	0.477464	0.088760	0.476564	0.630	0.19
16	0.44320	1.8750	30	0.088462	0.478381	0.089033	0.477592	0.640	0.17
18	0.44320	1.6667	30	0.088666	0.475794	0.089245	0.475139	0.650	0.14
20	0.44320	1.5000	30	0.088830	0.470825	0.089416	0.470311	0.660	0.11
22	0.44320	1.3636	30	0.088964	0.464356	0.089556	0.463940	0.660	0.09
23.0769	0.44320	1.3000	30	0.089027	0.460472	0.089622	0.460082	0.660	0.08

Appendix C. Validation Based on the Original (ℓ, R) Parametrization

Before introducing the proposed dimensionless formulation, the dynamic behavior of the quay-crane system was investigated by directly varying the hoisting length ℓ and the ISO-container mass-center-to-spreader distance R.

For the results reported in Table A2, the spreader mass and the ISO-container mass were kept constant at

$$m_s = 6000 \text{ kg}, \qquad m = 22{,}000 \text{ kg},$$

whereas both ℓ and R were simultaneously varied throughout the operating domain considered in this work.

Table A2 reports the analytical natural frequencies, the frequencies extracted from the Simscape Multibody model, and the corresponding relative errors for the complete set of simulated configurations.

Table A2. Comparison between the analytical natural frequencies and the frequencies identified from the Simscape Multibody model for the original (R, ℓ) parameterization.

R (m)	ℓ (m)	f_1 (Hz)	f_2 (Hz)	$f_{1,a}$ (Hz)	$f_{2,a}$ (Hz)	Error f_1 (%)	Error f_2 (%)
1.295	10	0.146484	0.500488	0.147674	0.589609	0.810	15.12
1.295	15	0.122070	0.491333	0.123233	0.576894	0.940	14.83
1.295	20	0.106812	0.488281	0.107893	0.570637	1.000	14.43
1.295	25	0.097656	0.485229	0.097135	0.566918	0.540	14.41
1.295	30	0.088501	0.482178	0.089059	0.564455	0.630	14.58
1.795	10	0.143433	0.540161	0.144575	0.709040	0.790	23.82
1.795	15	0.122070	0.524902	0.121403	0.689431	0.550	23.86
1.795	20	0.106812	0.518799	0.106655	0.679622	0.150	23.66
1.795	25	0.097656	0.515747	0.096228	0.673740	1.480	23.45
1.795	30	0.088501	0.512695	0.088358	0.669822	1.126	23.46
2.295	10	0.140381	0.552368	0.141656	0.818258	0.900	32.49
2.295	15	0.119019	0.537109	0.119650	0.790981	0.530	32.10
2.295	20	0.106812	0.527954	0.105459	0.777189	1.280	32.07
2.295	25	0.094604	0.524902	0.095346	0.768869	0.780	31.73
2.295	30	0.088501	0.521851	0.087673	0.763306	0.940	31.63

Table A2. *Cont.*

R (m)	ℓ (m)	f_1 (Hz)	f_2 (Hz)	$f_{1,a}$ (Hz)	$f_{2,a}$ (Hz)	Error f_1 (%)	Error f_2 (%)
2.795	10	0.140381	0.555420	0.138902	0.920907	1.060	39.69
2.795	15	0.119019	0.537109	0.117970	0.885334	0.890	39.33
2.795	20	0.103760	0.524902	0.104301	0.867202	0.520	39.47
2.795	25	0.094604	0.521851	0.094487	0.856213	0.120	39.05
2.795	30	0.088501	0.515747	0.087003	0.847003	1.720	39.24
3.295	10	0.137329	0.549316	0.136300	1.018979	0.760	46.09
3.295	15	0.115967	0.527954	0.116358	0.974584	0.340	45.83
3.295	20	0.103760	0.518799	0.103180	0.951806	0.560	45.49
3.295	25	0.094604	0.509644	0.093651	0.937949	1.020	45.66
3.295	30	0.085449	0.506592	0.086349	0.928630	1.040	45.45

Appendix D. Residual-Vibration Results over the Physical Parameter Sweep

Table A3 reports the peak-to-peak residual-vibration amplitudes obtained from the Simscape Multibody simulations for the complete sweep of the physical parameters ℓ and R. For each of the 25 operating configurations, the response obtained with the unshaped trolley command is compared with that obtained using the Convolved Unity Magnitude shaped command. The residual-vibration reduction is computed with respect to the corresponding unshaped response.

Table A3. Peak-to-peak residual-vibration amplitudes obtained for the unshaped and Convolved Unity Magnitude shaped commands over the complete (ℓ, R) parameter sweep.

R [m]	ℓ [m]	Unshaped [m]	Convolved Shaped [m]	Reduction [%]
1.295	10	3.956	0.507000	87.18
1.295	15	0.583	0.019700	96.62
1.295	20	4.587	0.134580	97.07
1.295	25	7.984	0.215500	97.30
1.295	30	10.742	1.026000	90.45
1.795	10	3.191	0.422757	86.75
1.795	15	0.803054	0.030894	96.15
1.795	20	4.892	0.128679	97.37
1.795	25	8.240	0.251544	96.95
1.795	30	10.952	1.102000	89.94
2.295	10	3.052	0.315171	89.67
2.295	15	1.184	0.046887	96.04
2.295	20	5.195	0.119253	97.70
2.295	25	8.516	0.312152	96.33
2.295	30	11.182	1.180000	89.45
2.795	10	2.792	0.224613	91.95
2.795	15	1.514	0.062518	95.87
2.795	20	5.506	0.106593	98.06
2.795	25	8.763	0.364116	95.84
2.795	30	11.411	1.261000	88.95
3.295	10	2.500	0.150497	93.98
3.295	15	1.859	0.078553	95.77
3.295	20	5.789	0.090580	98.44
3.295	25	9.035	0.422167	95.33
3.295	30	11.540	1.344000	88.35

References

1. Bartosek A.; Marek, O. Quay Cranes in Container Terminals. *Trans. Transf. Sci.* **2013**, *6*, 9. https://doi.org/10.2478/v10158-012-0027-y.
2. Louda, M.A.; Rye, D.C.; Dissanayake, M.W.M.G.; Durrant-Whyte, H.F. Identification of Load Sway in Quay-Cranes. In *Field and Service Robotics*; Springer: London, UK, 1998. https://doi.org/10.1007/978-1-4471-1273-0_58.
3. Masoud, Z.; Nayfeh, A.H. Sway Reduction on Container Cranes Using Delayed Feedback Controller. In Proceeding of the AIAA 2002, Reno, NV, USA, 14–17 January 2002.
4. Masoud, Z.N. Effect of hoisting cable elasticity on anti-sway controllers of quay-side container cranes. *Nonlinear Dyn.* **2009**, *58*, 129–140
5. Singer, N.C.; Seering, W.P. Preshaping Command Inputs to Reduce System Vibration. *ASME J. Dyn. Syst. Meas. Control* **1990**, *112*, 76–82. doi 10.1115/1.2894142.
6. Singhose, W.E.; Porter, L.; Kenison, M.; Kriikku, E. Effects of hoisting on the input shaping control of gantry cranes. *Control Eng. Pract.* **2000**, *8*, 1159–1165.
7. Lewis, D.; Parker, G.G.; Driessen, B.; Robinett, R.D. Command shaping control of an operator-in-the-loop boom crane. In Proceedings of the 1998 American Control Conference, Philadelphia, PA, USA, 24–26 June 1998; Volume 5. https://doi.org/10.1109/ACC.1998.688328.
8. Smith, O.J.M. Posicast control of damped oscillatory systems. *Proc. IRE* **1957**, *45*, 1249–1255. https://doi.org/10.1109/JRPROC.1957.278530.
9. Singer, N.C.; Seering, W.P. An extension of Command Shaping Methods for Controlling Residual Vibration Using Frequency Sampling. In Proceedings of the IEEE International Conference on Robotics and Automation, Nice, France, 12–14 May 1992; Volume 1, pp. 800–805.
10. Singhose, W.E.; Porter, L.J.; Tuttle, T.D.; Singer, N.C. Vibration Reduction Using Multi-Hump Input Shapers. *J. Dyn. Syst. Meas. Control* **1997**, *119*, 320–326.
11. Peláez, G.; Vaugan, J.; Izquierdo, P.; Rubio, H.; García-Prada, J.C. Dynamics and Embedded Internet of Things Input Shaping Control for Overhead Cranes Transporting Multibody Payloads. *Sensors* **2018**, *18*, 1817. https://doi.org/10.3390/s18061817.
12. Singhose, W. Command shaping for flexible systems: A review of the first 50 years. *Int. J. Precis. Eng. Manuf.* **2009**, *10*, 153–168.
13. Singh, T. (2009). *Optimal Reference Shaping for Dynamical Systems: Theory and Applications*; CRC Press: Boca Raton, FL, USA, 2009.
14. Peláez, G.; Izquierdo, P.; Peláez, Gustavo, Rubio, H. Learning-Augmented Input Shaping for Boom Cranes under Operational Constraints: A Real-World Implementation. *J. Vib. Control* 2026, *in press*.
15. Singhose, W.E.; Kenison M. Input Shaping Design for Double-Pendulum Planar Gantry Cranes. In Proceedings of the 1999 IEEE International Conference on Control Applications, Kohala Coast, HI, USA, 22–27 August 1999. https://doi.org/10.1109/CCA.1999.806702.
16. Johns, B.; Abdi, E.; Arashpour, M. Dynamical modelling of boom tower crane rigging systems: Model selection for construction. *Arch. Civ. Mech. Eng.* **2023**, *23*, 162. https://doi.org/10.1007/s43452-023-00702-x.
17. Nikravesh, P. *Planar Multibody Dynamics: Formulation, Programming and Applications*; CRC Press Taylor and Francis Group: Boca Raton, FL, USA, 2008; pp. 364–365
18. Pao, L.; Singhose, W.E. Unity Magnitude Input Shaper and Their Relation to Time Optimal. *IFAC Proc. Vol.* **1996**, *29*, 385–390. https://doi.org/10.1016/S1474-6670(17)57692-2.